

The Development of the North Pacific Jet Phase Diagram as an Objective Tool to Monitor the State and Forecast Skill of the Upper-Tropospheric Flow Pattern

ANDREW C. WINTERS, DANIEL KEYSER, AND LANCE F. BOSART

Department of Atmospheric and Environmental Sciences, University at Albany, State University of New York, Albany, New York

(Manuscript received 21 June 2018, in final form 17 December 2018)

ABSTRACT

Previous studies employing empirical orthogonal function (EOF) analyses of upper-tropospheric zonal wind anomalies have identified the leading modes of North Pacific jet (NPJ) variability that prevail on synoptic time scales. The first mode corresponds to a zonal extension or retraction of the exit region of the climatological NPJ, while the second mode corresponds to a poleward or equatorward shift of the exit region of the climatological NPJ. These NPJ regimes can strongly influence the character of the large-scale flow pattern over North America. Consequently, knowledge of the prevailing NPJ regime and the forecast skill associated with each NPJ regime can add considerable value to operational medium-range (6–10-day) forecasts over North America. This study documents the development of an NPJ phase diagram, which is constructed from the two leading EOFs of 250-hPa zonal wind anomalies during 1979–2014 excluding the summer months (June–August). The projection of 250-hPa zonal wind anomalies at one or multiple times onto the NPJ phase diagram provides an objective characterization of the state or evolution of the upper-tropospheric flow pattern over the North Pacific with respect to the two leading EOFs. A 30-yr analysis of GEFS reforecasts with respect to the NPJ phase diagram demonstrates that forecasts verified during jet retraction and equatorward shift regimes are associated with significantly larger average errors than jet extension and poleward shift regimes. An examination of the best and worst forecasts further suggests that periods characterized by rapid NPJ regime transition and the development and maintenance of North Pacific blocking events exhibit reduced forecast skill.

1. Introduction

Anchored downstream of the Asian continent at midlatitudes, the North Pacific jet (NPJ) stream is a narrow, meandering current of strong upper-tropospheric wind speeds bounded by appreciable horizontal and vertical shear. The position and intensity of the NPJ is modulated by a number of external factors, including tropical convection (e.g., Hoskins and Karoly 1981; Madden and Julian 1994; Harr and Dea 2009; Archambault et al. 2013, 2015; Torn and Hakim 2015; Grams and Archambault 2016; Bosart et al. 2017), interactions between the NPJ and baroclinic eddies along the midlatitude storm track (e.g., Orlanski and Sheldon 1995; Chang et al. 2002; Hakim 2003; Torn and Hakim 2015; Bosart et al. 2017), and the East Asian winter monsoon (e.g., Jhun and Lee 2004; Lee et al. 2010; Wang and Chen 2014; Handlos and Martin 2016). In combination, these factors contribute to

NPJ configurations that vary substantially on both weather and climate time scales.

In an attempt to characterize the variability of the NPJ, prior work has identified the leading modes of NPJ variability that prevail on weather and climate time scales during the winter (December–February). Schubert and Park (1991) provided one of the first investigations of subseasonal NPJ variability, and calculated the two leading traditional empirical orthogonal functions¹ (EOFs) of 20–70-day filtered zonal wind at 200 hPa over the Pacific basin. Their first EOF describes the variability in the intensity of the NPJ over the western North Pacific, while their second EOF describes a zonal extension or retraction of the exit region of the climatological NPJ. In contrast, Eichelberger and Hartmann (2007) employed daily zonal wind data during January in their traditional

Corresponding author: Andrew C. Winters, acwinters@albany.edu

¹ A traditional EOF analysis is a statistical technique to extract patterns that explain the greatest fraction of the variance within a multidimensional dataset (Wilks 2011, chapter 12).

EOF analysis and found that the first EOF of the vertically averaged zonal-mean zonal wind over the North Pacific encompasses variability in the intensity, longitudinal extent, and latitudinal position of the NPJ. Consequently, the [Eichelberger and Hartmann \(2007\)](#) analysis suggests that NPJ variability is considerably more complex when analyzed on synoptic rather than subseasonal time scales.

Recent studies by [Athanasiadis et al. \(2010\)](#) and [Jaffe et al. \(2011\)](#) provided additional physical clarity on the two leading modes of NPJ variability that prevail on synoptic time scales during the cold season (November–March). These studies applied traditional EOF analysis to unfiltered upper-tropospheric zonal wind data over the North Pacific and determined that the first mode of NPJ variability corresponds to longitudinal variability in the vicinity of the exit region of the climatological NPJ. Specifically, a positive EOF 1 pattern (+EOF 1) describes a zonal extension of the exit region of the climatological NPJ, while a negative EOF 1 pattern (−EOF 1) describes a zonal retraction of the exit region of the climatological NPJ. The second mode of NPJ variability corresponds to latitudinal variability in the vicinity of the exit region of the climatological NPJ. Within the context of this mode, a positive EOF 2 pattern (+EOF 2) describes a poleward shift of the exit region of the climatological NPJ, while a negative EOF 2 pattern (−EOF 2) describes an equatorward shift.

Knowledge of the four NPJ configurations identified by [Athanasiadis et al. \(2010\)](#) and [Jaffe et al. \(2011\)](#), hereafter referred to as NPJ regimes, subsequently permits an examination of the relationship between each NPJ regime and the downstream large-scale flow pattern over North America. To this end, [Griffin and Martin \(2017\)](#) employed time-extended EOF analyses (e.g., [Weare and Nasstrom 1982](#); [Wilks 2011](#), chapter 12) of 250-hPa zonal wind data from the NCEP–NCAR reanalysis dataset ([Kalnay et al. 1996](#)) to construct composite analyses of the large-scale flow evolution over the North Pacific and North America during the 10-day period preceding and following the development of each NPJ regime. The [Griffin and Martin \(2017\)](#) analysis yields a clear relationship between each NPJ regime and the large-scale flow pattern over North America, and implies that knowledge of the prevailing NPJ regime may add considerable value to operational medium-range (6–10-day) forecasts of temperature and precipitation over North America. However, this value is limited operationally without complementary knowledge of the relative forecast skill associated with the development or persistence of each NPJ regime.

The concept of regime-dependent forecast skill has been explored with respect to large-scale upper-tropospheric flow regimes over the North Atlantic basin (e.g., [Ferranti et al. 2015](#)) and with respect to large-scale atmospheric teleconnection patterns (e.g., [Palmer 1988](#);

[Lin and Derome 1996](#); [Sheng 2002](#); [Ferranti et al. 2015](#)). While the configuration of midlatitude jet streams can be closely related to atmospheric teleconnection patterns (e.g., [Wettstein and Wallace 2010](#); [Woollings et al. 2010](#); [Madonna et al. 2017](#)), a study that examines regime-dependent forecast skill over the North Pacific with respect to the leading modes of NPJ variability on synoptic time scales has not been conducted. Consequently, a primary goal of the present study is to identify whether certain NPJ regimes exhibit enhanced or reduced forecast skill. In an effort to address this goal, the results from prior studies on NPJ variability (e.g., [Athanasiadis et al. 2010](#); [Jaffe et al. 2011](#); [Griffin and Martin 2017](#)) are extended to the cool season (September–May) and a two-dimensional phase diagram, hereafter referred to as the NPJ phase diagram, is developed employing the two leading modes of NPJ variability during that time period. The NPJ phase diagram subsequently aids in visualizing the state and evolution of the upper-tropospheric flow pattern over the North Pacific, and serves as an objective tool from which new insights can be derived regarding the climatology and forecast skill of each NPJ regime.

The remainder of this manuscript is structured as follows. [Section 2](#) discusses the development of the NPJ phase diagram. [Section 3](#) discusses the climatology of each NPJ regime and reviews the large-scale flow patterns associated with each NPJ regime. [Section 4](#) examines the forecast skill of each NPJ regime with respect to the NPJ phase diagram. [Section 5](#) illuminates the characteristics of the best and worst medium-range forecast periods with respect to the NPJ phase diagram, and [section 6](#) offers a discussion of the results and some conclusions.

2. Development of the NPJ phase diagram

The NPJ phase diagram is developed utilizing anomalies of the zonal component of the 250-hPa vector wind from the 0.5°-resolution National Centers for Environmental Prediction Climate Forecast System Reanalysis (CFSR; [Saha et al. 2010, 2014](#)) at 6-h intervals during 1979–2014 excluding the summer months (June–August). The CFSR is chosen for this study because of its role in providing the initial conditions for the Global Ensemble Forecast System (GEFS) Reforecast version 2 dataset prior to 2011 ([Hamill et al. 2013](#)). The GEFS Reforecast dataset is utilized in [sections 4](#) and [5](#) to examine the forecast skill of each NPJ regime with respect to the NPJ phase diagram. The 250-hPa zonal wind anomalies are calculated as the deviation of the instantaneous 250-hPa zonal wind from a 21-day running mean centered on each analysis time in order to remove the 36-yr mean as well as the annual and diurnal cycles. The 21-day running mean

at a particular analysis time is calculated from 250-hPa zonal wind data taken at 24-h intervals within a 21-day window centered on the analysis time for every year during 1979–2014. A traditional EOF analysis (Wilks 2011, chapter 12) is subsequently performed on the 250-hPa zonal wind anomaly data² within a horizontal domain bounded in latitude from 10° to 80°N and in longitude from 100°E to 120°W in order to identify the two leading modes of NPJ variability. This horizontal domain is chosen to encompass the North Pacific basin and to match the domain employed by Griffin and Martin (2017).

In comparison to traditional EOF analysis, Griffin and Martin (2017) demonstrate that time-extended EOF analysis (e.g., Weare and Nasstrom 1982; Wilks 2011, chapter 12) of 250-hPa zonal wind anomalies over the North Pacific is beneficial for ensuring that the evolution of the NPJ is characterized by a higher degree of temporal coherence. However, this higher degree of temporal coherence is achieved by filtering out the high-frequency variability of the NPJ that occurs on daily time scales (Griffin and Martin 2017, their Fig. 1). When considering the NPJ and its influence on the downstream upper-tropospheric flow pattern over North America, short-term fluctuations in the position, intensity, and evolution of the NPJ, such as those associated with recurving tropical cyclones or intensifying extratropical cyclones, can have substantial impacts on the character of the downstream upper-tropospheric flow pattern over North America (e.g., Archambault et al. 2015; Torn and Hakim 2015; Grams and Archambault 2016; Bosart et al. 2017). Additionally, the application of time-extended EOF analysis is computationally more expensive than traditional EOF analysis, especially when employing a dataset with 0.5° resolution such as the CFSR. For these two reasons, traditional EOF analysis is chosen for this study. The subsequent analysis demonstrates that the application of traditional EOF analysis to 250-hPa zonal wind anomalies from the CFSR during the cool season produces the same two leading modes of NPJ variability as were found in previous studies (Athanasiadis et al. 2010; Jaffe et al. 2011; Griffin and Martin 2017).

The regression of 250-hPa zonal wind anomaly data from the CFSR onto the first two standardized principal components (PCs), PC 1 and PC 2, obtained from the traditional EOF analysis reveals the spatial structures of EOF 1 and EOF 2 (Figs. 1a and 1b, respectively). EOF 1 explains 10.3% of the variance of 250-hPa zonal wind over the North Pacific and corresponds to the

longitudinal variability of the 250-hPa zonal wind in the vicinity of the exit region of the climatological NPJ. A positive EOF 1 pattern (+EOF 1) is associated with a zonal extension of the exit region of the climatological NPJ (i.e., a jet extension), while a negative EOF 1 pattern (−EOF 1) is associated with a retraction of the exit region of the climatological NPJ (i.e., a jet retraction). EOF 2 explains 7.8% of the variance of 250-hPa zonal wind over the North Pacific and corresponds to latitudinal variability of the 250-hPa zonal wind in the vicinity of the exit region of the climatological NPJ. A positive EOF 2 pattern (+EOF 2) is associated with a poleward shift of the exit region of the climatological NPJ (i.e., a poleward shift), while a negative EOF 2 pattern (−EOF 2) is associated with an equatorward shift of the exit region of the climatological NPJ (i.e., an equatorward shift). The combined variance explained by EOF 1 and EOF 2 is comparable to that found in previous studies (Athanasiadis et al. 2010; Jaffe et al. 2011; Griffin and Martin 2017) and the two leading EOFs are statistically well separated using the methodology outlined in North et al. (1982). To ensure that the EOF patterns shown in Fig. 1 are representative of the entire cool season, separate traditional EOF analyses were performed on 3-month subsets of the 250-hPa zonal wind anomaly data. These independent EOF analyses (not shown) confirm that EOF 1 and EOF 2 represent the two leading modes of NPJ variability with fidelity throughout the cool season.

The magnitudes and signs of PC 1 and PC 2 are normalized to unit variance, and time series constructed from the instantaneous PCs assist in characterizing the temporal evolution of the NPJ with respect to EOF 1 and EOF 2. As noted by Griffin and Martin (2017), the use of instantaneous PCs produces a noisy time series due to the high-frequency variability that characterizes the NPJ on daily time scales (their Fig. 1). Consequently, in an attempt to describe the evolution of the NPJ with greater temporal coherence than the instantaneous PCs while preserving the high-frequency variability of the NPJ on daily time scales, the instantaneous PCs are smoothed through the calculation of a weighted average of the instantaneous PCs within ± 24 h of each analysis time t_0 . The weight w prescribed to the instantaneous PCs at each analysis time t within ± 24 h of t_0 is defined as $w = 5 - |t - t_0|/6$, for $|t - t_0| \leq 24$ h.

The weighted PCs at a particular analysis time can be plotted onto a two-dimensional Cartesian grid (i.e., the NPJ phase diagram) in an effort to visualize the state of the NPJ. The position along the abscissa within the NPJ phase diagram corresponds to the value of weighted PC 1 and indicates how strongly the 250-hPa zonal wind anomalies project onto EOF 1. Positive and negative

² The 250-hPa zonal wind anomalies are weighted by the square root of their associated grid cell area prior to the application of traditional EOF analysis.

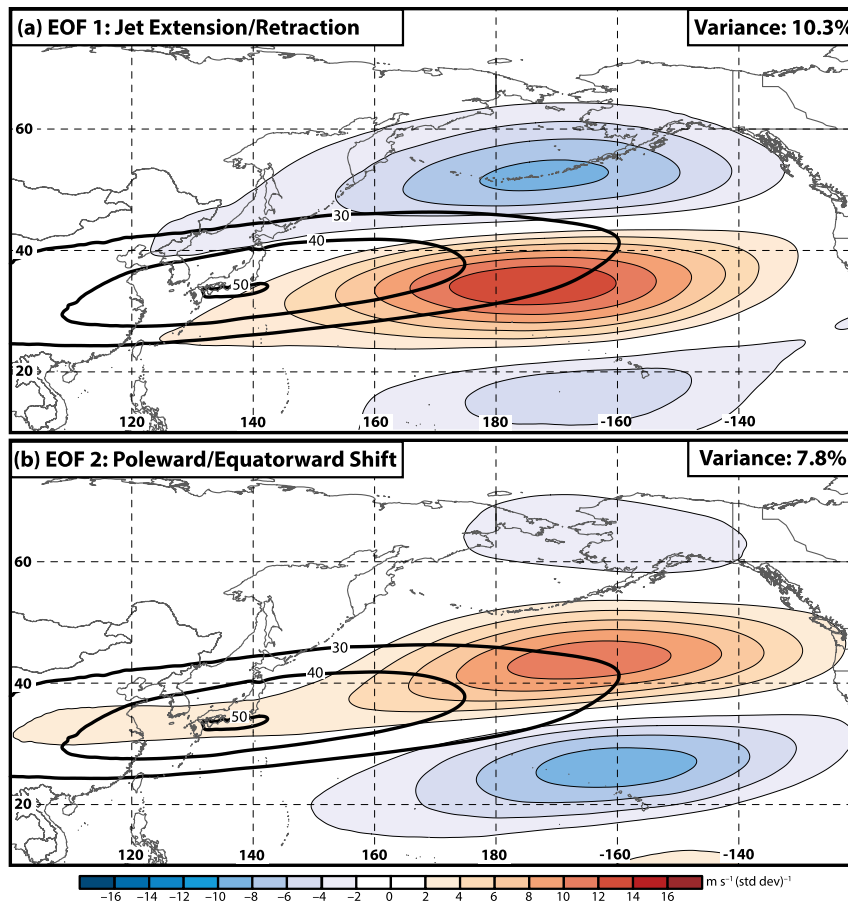


FIG. 1. (a) September–May 250-hPa mean zonal wind is contoured in black every 10 m s^{-1} above 30 m s^{-1} , and the regression of 250-hPa zonal wind anomaly data onto standardized PC 1 (i.e., EOF 1) is shaded (m s^{-1}). The variance of 250-hPa zonal wind during the cool season that is explained by EOF 1 is listed in the top right of the panel. (b) As in (a), but for the regression of 250-hPa zonal wind anomaly data onto standardized PC 2 (i.e., EOF 2).

values of weighted PC 1 represent a jet extension and jet retraction, respectively. The position along the ordinate within the NPJ phase diagram corresponds to the value of weighted PC 2 and indicates how strongly the 250-hPa zonal wind anomalies project onto EOF 2. Positive and negative values of weighted PC 2 represent a poleward shift and an equatorward shift, respectively.

Examples of NPJ configurations that project strongly onto a jet extension and a jet retraction regime are provided in Figs. 2a and 2c, respectively, while NPJ configurations that project strongly onto a poleward shift and an equatorward shift regime are provided in Figs. 3a and 3c, respectively. Considering these sample NPJ configurations, it is important to note that the upper-tropospheric flow pattern at any one time is considerably more complex than that implied by the NPJ phase diagram and the EOF patterns shown in Fig. 1. Nevertheless, given that the NPJ phase diagram is constructed from the two

leading modes of 250-hPa zonal wind variability over the North Pacific during the cool season, plotting the weighted PCs on the NPJ phase diagram and tracking their evolution over time encompasses many important aspects of the NPJ and its evolution.

As for the sample cases shown in Figs. 2 and 3, the weighted PCs at all analysis times during 1979–2014 excluding the summer months are plotted on the NPJ phase diagram in order to classify each analysis time into one of the four NPJ regimes, or to identify analysis times during which the NPJ lies within the unit circle (Fig. 4). For this classification scheme, the analysis times are classified based on, first, whether the position of the NPJ within the NPJ phase diagram is greater than a distance of one standard deviation from the origin and, second, whether the absolute value of PC 1 or PC 2 is greater. Analysis times that fall into the “origin” category are interpreted as times during which the NPJ exhibits a structure not far

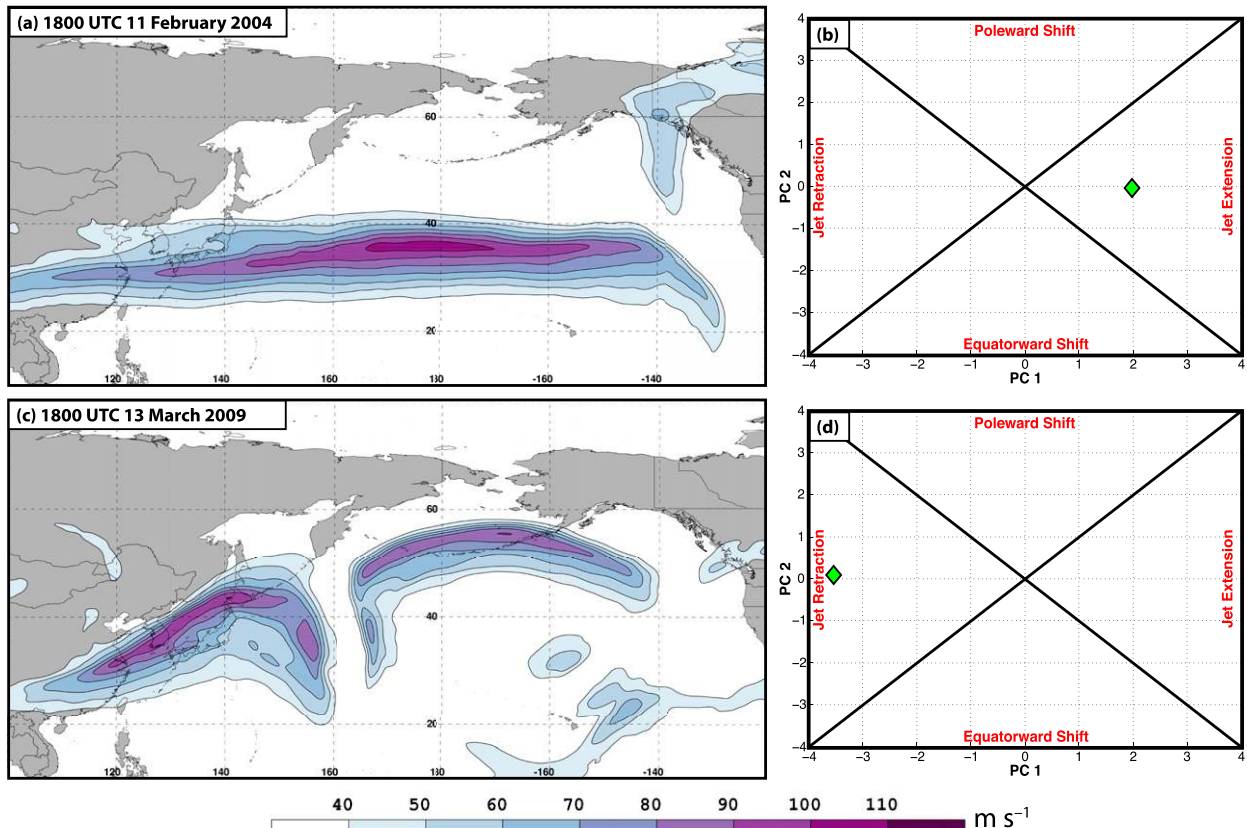


FIG. 2. (a) The 250-hPa wind speed (m s^{-1}) is shaded following the legend at 1800 UTC 11 Feb 2004. (b) The location of weighted PC 1 and PC 2 at 1800 UTC 11 Feb 2004 within the NPJ phase diagram. (c),(d) As in (a),(b), but at 1800 UTC 13 Mar 2009.

from climatology, or at least a structure that does not project strongly onto EOF 1 and EOF 2. Plotting the weighted PCs onto the NPJ phase diagram over a specified time interval yields a trajectory within the NPJ phase diagram that describes the evolution of the NPJ.

3. Characteristics of the NPJ phase diagram

The classification of analysis times discussed in section 2 reveals several salient characteristics of each NPJ regime. The number of analysis times characterized by each NPJ regime and the typical residence time of the NPJ within each NPJ regime are provided in Table 1. Overall, the mean and median residence times within an NPJ regime do not vary considerably between the NPJ regimes. Specifically, the mean residence time within an NPJ regime ranges between 3.58 and 3.85 days, while the median residence time ranges

between 2.50 and 2.75 days.³ The residence time is slightly longer for periods during which the NPJ resides within one standard deviation of the origin in the NPJ phase diagram, with mean and median residence times of 4.65 and 3.25 days, respectively. The mean residence time is larger than the median for each NPJ regime, which highlights the degree to which the distribution of residence times is positively skewed toward a few persistent, long-lasting NPJ regimes. In support of this observation, an examination of the minimum and maximum residence times within each NPJ regime indicates that while an NPJ regime can be transient, it can also persist for multiple weeks.

As demonstrated from previous studies on NPJ variability, each NPJ regime exhibits a strong influence on the character of the downstream large-scale flow pattern over North America (e.g., Athanasiadis et al. 2010; Jaffe et al. 2011; Griffin and Martin 2017). To ensure consistency with previous studies, composite analyses are constructed employing the CFSR for periods during which the NPJ resided within the same NPJ regime for at least three consecutive days. A 3-day threshold is chosen as a compromise between the magnitude of the mean and median residence times for each NPJ regime (Table 1).

³The mean and median residence times shown in Table 1 are sensitive to the smoothing procedure described in section 2. The use of instantaneous PCs yields mean and median residence times that are approximately a day shorter than those discussed in the text.

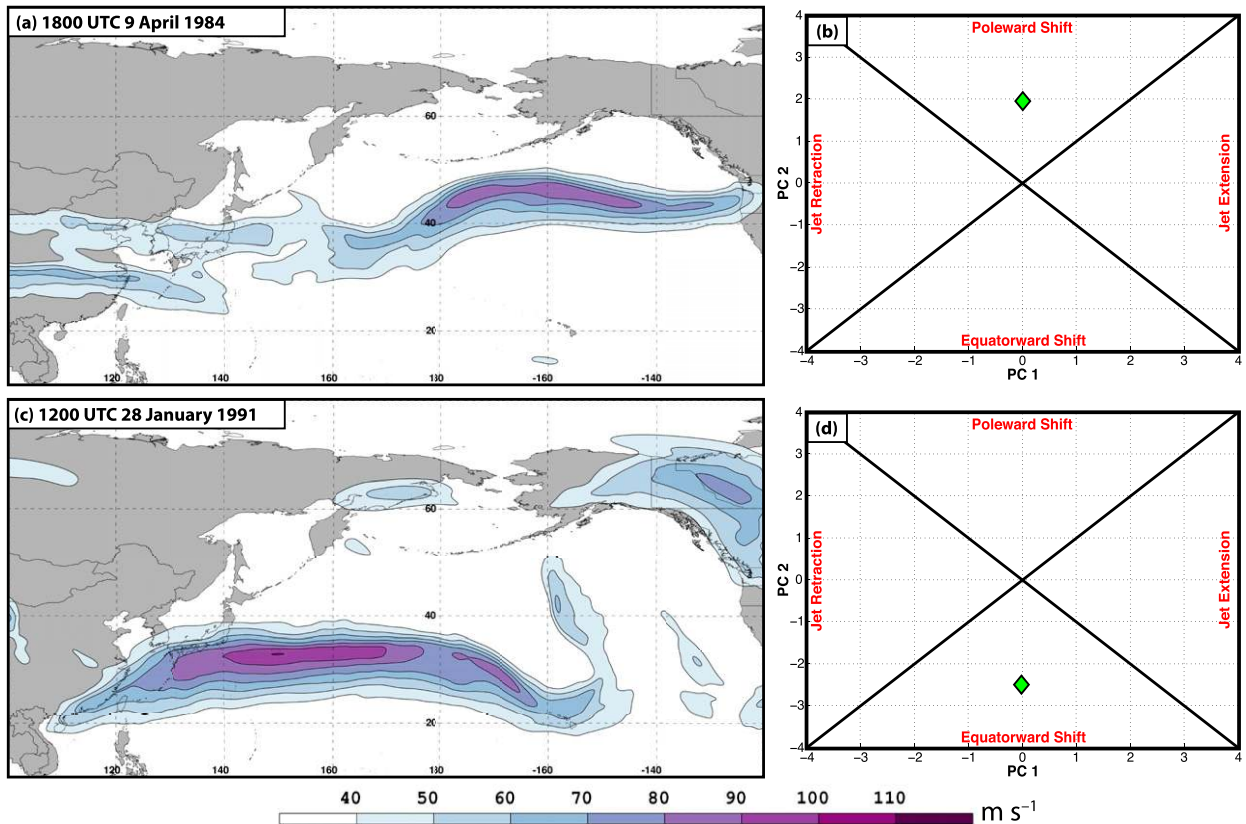


FIG. 3. As in Fig. 2, but at (a),(b) 1800 UTC 9 Apr 1984 and (c),(d) 1200 UTC 28 Jan 1991.

Figure 5 illustrates the characteristic large-scale flow pattern 4 days following the onset of each NPJ regime. A 4-day time lag is chosen to highlight both the characteristic structure of the NPJ as well as the downstream flow pattern over North America associated with each NPJ regime. Two-sided Student's t tests were performed on the geopotential height and temperature anomaly fields shown in Fig. 5 to identify anomalies that are statistically distinct from climatology at the 99% confidence level.

A jet extension is characterized by the meridional juxtaposition of an anomalous upper-tropospheric trough over the central North Pacific and an anomalous ridge over the subtropical North Pacific that combine to produce a strong, zonally oriented NPJ (Fig. 5a). Beneath the left-exit region of the extended NPJ, an anomalous surface cyclone induces anomalous southerly geostrophic flow along the west coast of North America (Fig. 5b). This southerly geostrophic flow is collocated with lower-tropospheric warm anomalies over western North America as well as an anomalous upper-tropospheric ridge in the same location (Fig. 5a). Lower-tropospheric cold anomalies are found upstream of the surface cyclone in association with anomalous northerly geostrophic flow over the central North Pacific, and across

eastern North America beneath an anomalous upper-tropospheric trough (Fig. 5b).

A jet retraction features upper- and lower-tropospheric patterns that are largely opposite of those observed for

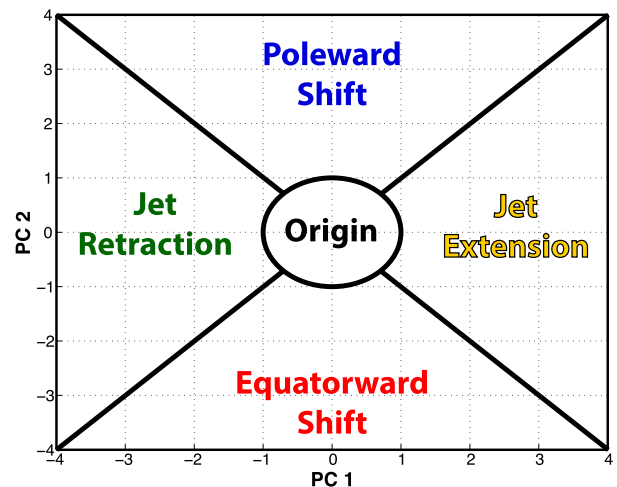


FIG. 4. Schematic illustrating the classification scheme for CFSR analysis times and GEFS reforecasts with respect to the NPJ phase diagram.

TABLE 1. Characteristic residence times (days) for each NPJ regime. The numbers in parentheses represent the number of analysis times characterized by each NPJ regime during 1979–2014 excluding the summer months (June–August).

NPJ regime	Mean residence time (days)	Median residence time (days)	Max residence time (days)	Min residence time (days)
Jet extension ($N = 5842$)	3.85	2.50	27.25	0.25
Jet retraction ($N = 5685$)	3.70	2.75	34.00	0.25
Poleward shift ($N = 6164$)	3.58	2.75	18.00	0.25
Equatorward shift ($N = 5437$)	3.65	2.50	18.50	0.25
Origin ($N = 16212$)	4.65	3.25	35.50	0.25

a jet extension. In particular, a jet retraction is associated with an anomalous upper-tropospheric ridge over the central North Pacific, as well as anomalous troughs over northwestern North America and the subtropical North Pacific (Fig. 5c). In combination, these geopotential height anomalies result in a retracted NPJ to the west of the date line. Directly beneath the central North Pacific ridge, the circulation concomitant with an anomalous surface anticyclone is associated with lower-tropospheric cold anomalies over Alaska and the west coast of North America, along with warm anomalies over the central North Pacific (Fig. 5d). Lower-tropospheric warm anomalies are also found in the south-central United States upstream of an anomalous upper-tropospheric ridge positioned over the southeastern United States.

A poleward shift exhibits an anomalous upper-tropospheric trough over the high-latitude North Pacific and an anomalous ridge over the subtropical North Pacific that act in combination to position the exit region of the NPJ poleward of 40°N (Fig. 5e). An anomalous surface cyclone is located beneath the left-exit region of the poleward-shifted NPJ, which results in anomalous southerly geostrophic flow within an area characterized by lower-tropospheric warm anomalies over northern North America (Fig. 5f). These lower-tropospheric warm anomalies are also associated with an anomalous upper-tropospheric ridge positioned over eastern Canada (Fig. 5e). Lower-tropospheric cold anomalies are only observed over the Bering Strait and Gulf of Alaska during a poleward shift in conjunction with anomalous northerly geostrophic flow upstream of the surface cyclone (Fig. 5f).

An equatorward shift features upper- and lower-tropospheric flow patterns that are largely opposite of those observed for a poleward shift. Specifically, an equatorward shift is associated with an anomalous upper-tropospheric ridge over the high-latitude North Pacific and an anomalous trough over the subtropical North Pacific (Fig. 5g), reminiscent of a Rex block (Rex 1950). This configuration of geopotential height anomalies results in an equatorward deflection of the exit region of the NPJ near the date line, and a weaker NPJ

over the western North Pacific compared to the other NPJ regimes. An anomalous upper-tropospheric trough is also positioned over eastern Canada downstream of the high-latitude ridge over the North Pacific (Fig. 5g). In the lower troposphere, an equatorward shift is associated with an anomalous surface anticyclone centered near the Aleutian Islands (Fig. 5h). This surface anticyclone induces anomalous northerly geostrophic flow within an area characterized by lower-tropospheric cold anomalies downstream of the surface anticyclone over northern North America. Conversely, anomalous southerly geostrophic flow upstream of the surface anticyclone is associated with the presence of lower-tropospheric warm anomalies over the Bering Strait and the Gulf of Alaska.

Consideration of the interannual and intraseasonal variability of each NPJ regime offers insight into the characteristic structure of the NPJ. While the NPJ resides within one of the four NPJ regimes (i.e., outside a radius of one standard deviation from the origin) 59% of the time during an average cool season (not shown), there is considerable interannual variability in the frequency of each NPJ regime (Fig. 6a). As an example, the 1997/98 cool season was characterized by the second-lowest annual frequency of poleward shifts (4.7%), while the subsequent 1998/99 cool season featured the highest annual frequency of poleward shifts (34.9%). Comparable abrupt changes in the annual frequency of an individual NPJ regime are readily observed when considering the time series for other NPJ regimes. Furthermore, linear regressions performed on each of the time series shown in Fig. 6a do not identify any statistically significant trends in the frequency of each NPJ regime during 1979–2014 (not shown).

There is considerable intraseasonal variability in the frequency of each NPJ regime, as well (Fig. 6b). Specifically, the NPJ resides within an NPJ regime most frequently during November–March and less frequently during the months of September, October, April, and May. Both jet extensions and jet retractions peak in frequency during the month of March, while poleward shifts and equatorward shifts peak during February and

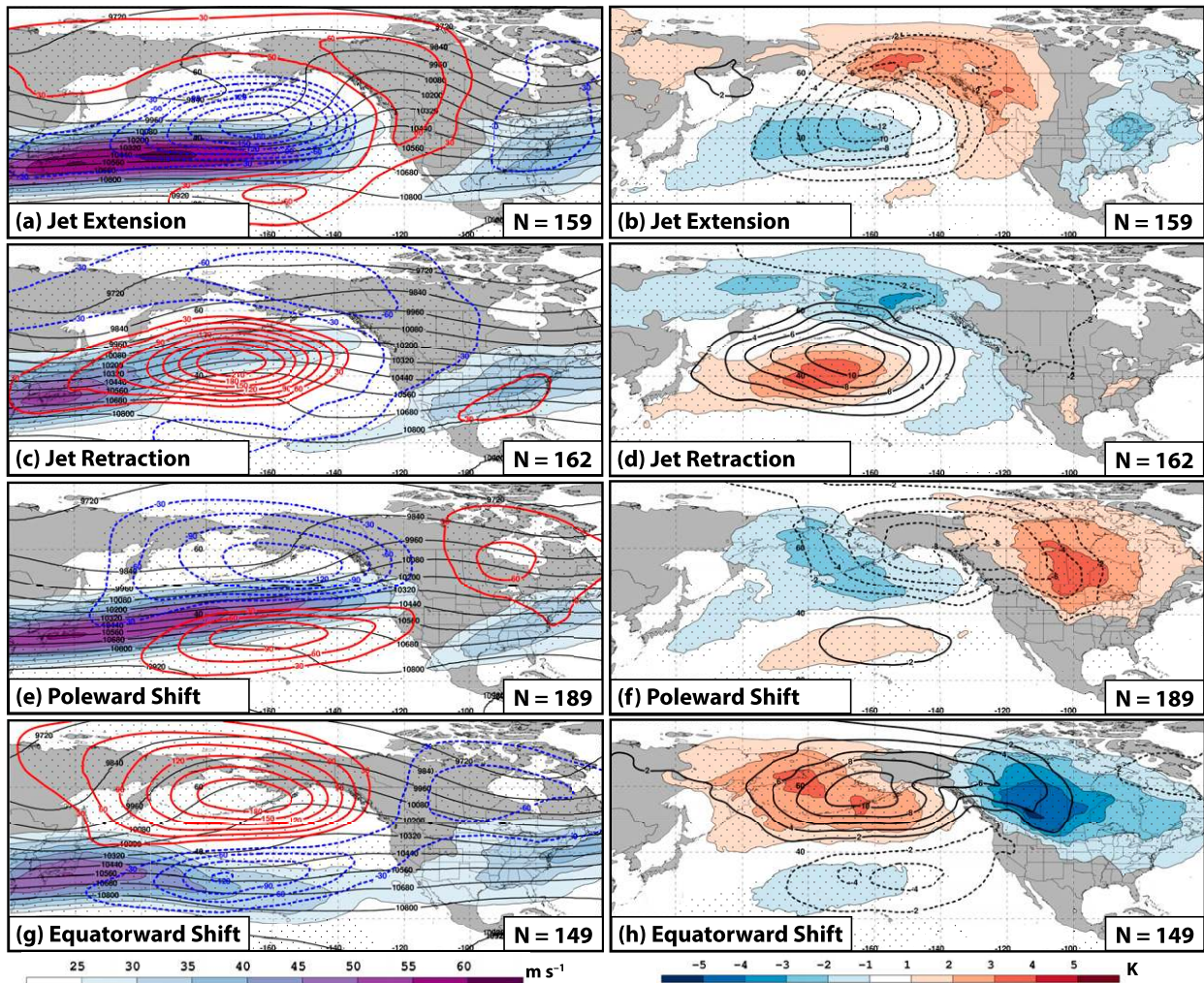


FIG. 5. Composite mean 250-hPa wind speed (m s^{-1}) is shaded in the fill pattern, 250-hPa geopotential height is contoured in black every 120 m, and 250-hPa geopotential height anomalies are contoured in solid red and dashed blue every 30 m for positive and negative values, respectively, 4 days following the initiation of (a) a jet extension, (c) a jet retraction, (e) a poleward shift, and (g) an equatorward shift regime. Composite anomalies of mean sea level pressure are contoured in solid and dashed black every 2 hPa for positive and negative values, respectively, and 850-hPa temperature anomalies are shaded in the bottom right of each panel indicate the number of cases included in each composite. Stippled areas represent locations where the 250-hPa geopotential height anomalies or 850-hPa temperature anomalies are statistically distinct from climatology at the 99% confidence level.

January, respectively. The frequencies of each NPJ regime during an individual month are generally comparable, except during March, when jet extensions and jet retractions are noticeably more frequent than poleward shifts and equatorward shifts, and during September, when poleward shifts and equatorward shifts are considerably more frequent than jet extensions and jet retractions.

As might be anticipated, the interannual and intra-seasonal frequencies of each NPJ regime are related to large-scale atmospheric teleconnection patterns. For example, the Pacific–North American (PNA) pattern is

known to be strongly related to the intensity of the NPJ (e.g., Wallace and Gutzler 1981; Barnston and Livezey 1987; Franzke and Feldstein 2005; Strong and Davis 2008; Athanasiadis et al. 2010; Wettstein and Wallace 2010; Franzke et al. 2011; Griffin and Martin 2017). Specifically, a positive PNA pattern is characterized by an anomalous upper-tropospheric trough over the central North Pacific and an anomalous ridge over the subtropical North Pacific. Consequently, a positive PNA pattern is conducive to an extended (Fig. 5a) or poleward-shifted NPJ (Fig. 5e). Conversely, a negative PNA pattern exhibits an anomalous upper-tropospheric

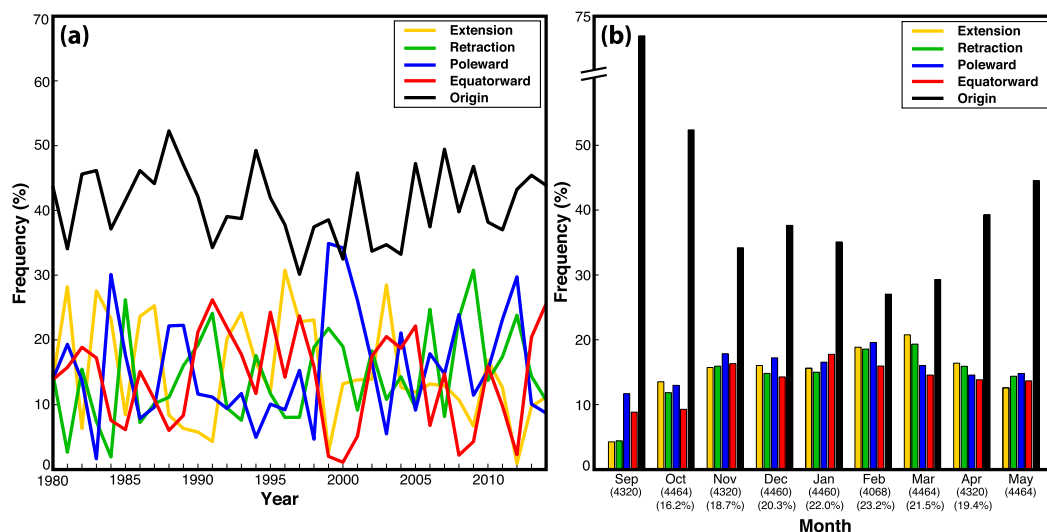


FIG. 6. (a) The percent frequency of analysis times during every cool season between September 1979 and May 2014 that are characterized by each NPJ regime. The years indicated along the horizontal axis identify the ends of individual cool seasons. (b) The percent frequency of analysis times during each month of the cool season that are characterized by each NPJ regime. The numbers in parentheses below each month indicate the number of analysis times during each month. The percentage in parentheses below a particular month identifies the amount of variance explained by the first two EOFs of 250-hPa zonal wind anomaly data during the 3-month period centered on that particular month between 1979 and 2014.

ridge over the central North Pacific, which favors a retracted (Fig. 5c) or equatorward-shifted NPJ (Fig. 5g).

To illustrate the relationship between the PNA and each NPJ regime, all analysis times that were characterized by an NPJ regime (i.e., outside a radius of one standard deviation from the origin) were classified based on the sign and magnitude of the daily PNA index (CPC 2017b). Analysis times that featured a PNA index > 0.5 (PNA index < -0.5) were classified as occurring during a positive (negative) PNA, and those remaining were classified as occurring during a neutral PNA. Figure 7a demonstrates that the frequency of each NPJ regime is well associated with the phase of the PNA. In particular, a positive PNA is most frequently characterized by jet extensions and poleward shifts, while a negative PNA is most frequently characterized by jet retractions and equatorward shifts.

The frequency of each NPJ regime also exhibits an association with the phase of the Arctic Oscillation (AO; e.g., Thompson and Wallace 1998; Higgins et al. 2000). The positive (negative) phase of the AO is characterized by above-normal (below normal) 1000-hPa geopotential heights over the central North Pacific and below-normal (above normal) 1000-hPa geopotential heights over the Arctic. As for the PNA index, daily AO indices (CPC 2017a) are employed to classify analysis times that were characterized by an NPJ regime. Analysis times exhibiting an AO index > 0.5 (AO index < -0.5) were classified as

occurring during a positive (negative) AO, and those remaining were classified as occurring during a neutral AO. Figure 7b indicates that a positive AO is most frequently characterized by jet retractions and a negative AO is most frequently characterized by jet extensions. This relationship agrees with the NPJ regime composites shown in Figs. 5d and 5b, given that jet retractions are associated with an anomalous surface anticyclone over the central North Pacific (Fig. 5d), and jet extensions feature an anomalous surface cyclone in that location (Fig. 5b).

The structure of the NPJ is also related to the El Niño–Southern Oscillation (ENSO). For example, prior work suggests that anomalous convection and above-normal sea surface temperatures over the central and eastern equatorial Pacific during an El Niño favor an extended or equatorward-shifted NPJ. Conversely, anomalous convection and above-normal sea surface temperatures over the western equatorial Pacific during La Niña favor a retracted or poleward-shifted NPJ (e.g., Horel and Wallace 1981; Rasmusson and Wallace 1983; Rasmusson and Mo 1993; Yang et al. 2002; Li and Wettstein 2012; Xie et al. 2015; Cook et al. 2017). In an effort to frame this relationship with respect to the NPJ phase diagram, analysis times that were characterized by an NPJ regime were classified based on the sign and magnitude of the monthly Niño-3.4 index (ESRL 2017). Analysis times that coincided with a Niño-3.4 index > 1.0 (Niño-3.4 index < -1.0) were classified as occurring during an El

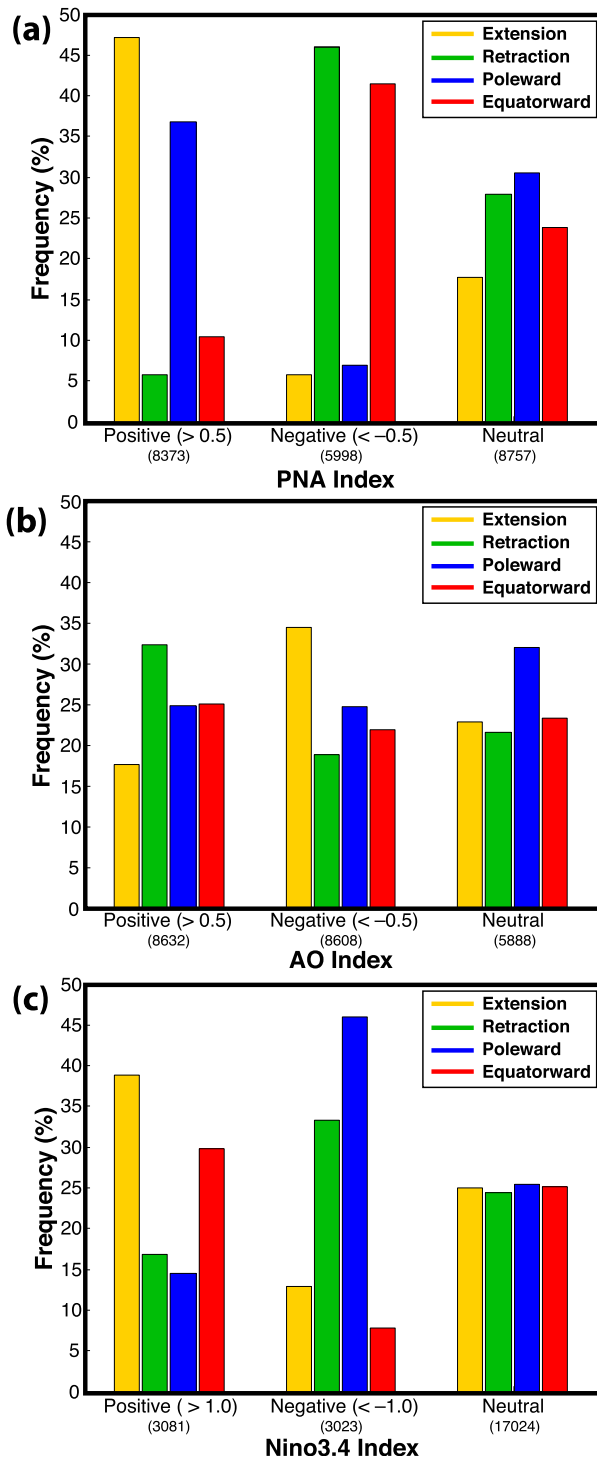


FIG. 7. (a) The percent frequency of each NPJ regime at analysis times during which the NPJ is outside of the unit circle on the NPJ phase diagram and characterized by each phase of the PNA discussed in the text. The numbers in parentheses below each category indicate the number of analysis times in each category. (b) As in (a), but for the AO. (c) As in (a), but for ENSO.

Niño (a La Niña), and those remaining were classified as occurring during a neutral ENSO state. Figure 7c demonstrates that El Niño is most frequently characterized by jet extensions and equatorward shifts. Conversely, La Niña is most frequently characterized by jet retractions and poleward shifts. The results from Fig. 7c translate to individual cool seasons characterized by El Niño and La Niña events, as well. For example, Fig. 6a indicates that the 1982–83 El Niño cool season (September–May Niño-3.4 = 1.82) was most frequently characterized by jet extensions and equatorward shifts, while the 1999–2000 La Niña cool season (September–May Niño-3.4 = -1.22) was most frequently characterized by jet retractions and poleward shifts.

4. GEFS forecast skill with respect to the NPJ phase diagram

Given the relationship between each NPJ regime and the downstream large-scale flow pattern over North America (Fig. 5), additional knowledge of the forecast skill associated with each NPJ regime offers the potential to increase confidence in operational medium-range forecasts over North America. To evaluate the forecast skill associated with each NPJ regime, an ensemble of 9-day forecast trajectories within the NPJ phase diagram is calculated daily during 1985–2014 excluding the summer months using 250-hPa zonal wind data from the 1.0°-resolution⁴ GEFS Reforecast version 2 dataset (Hamill et al. 2013). The GEFS Reforecast dataset features 10 ensemble member forecasts and 1 control member forecast initialized daily at 0000 UTC, each with forecast lead times as long as 384 h.

Forecast errors are defined with respect to the NPJ phase diagram and are calculated as the Euclidean distance error in standard deviations between the ensemble mean NPJ phase diagram forecast and the verifying 0-h analysis that corresponds to each forecast lead time. The NPJ phase diagram forecasts are then classified based on 1) the position of the NPJ within the NPJ phase diagram at the time of forecast initialization or forecast verification according to the schematic shown in Fig. 4 and 2) the season. Two-sided Student's *t* tests are performed on all NPJ phase diagram forecast error statistics to assess statistical significance in accordance with the specifications described in each pertinent figure caption. Recall from section 2 that the upper-tropospheric flow

⁴ While the GEFS Reforecast version 2 dataset is available at 1.0° resolution, the GEFS was run at a resolution of ~0.5° for week 1 reforecasts and a resolution of ~0.75° for week 2 reforecasts (Hamill et al. 2013).

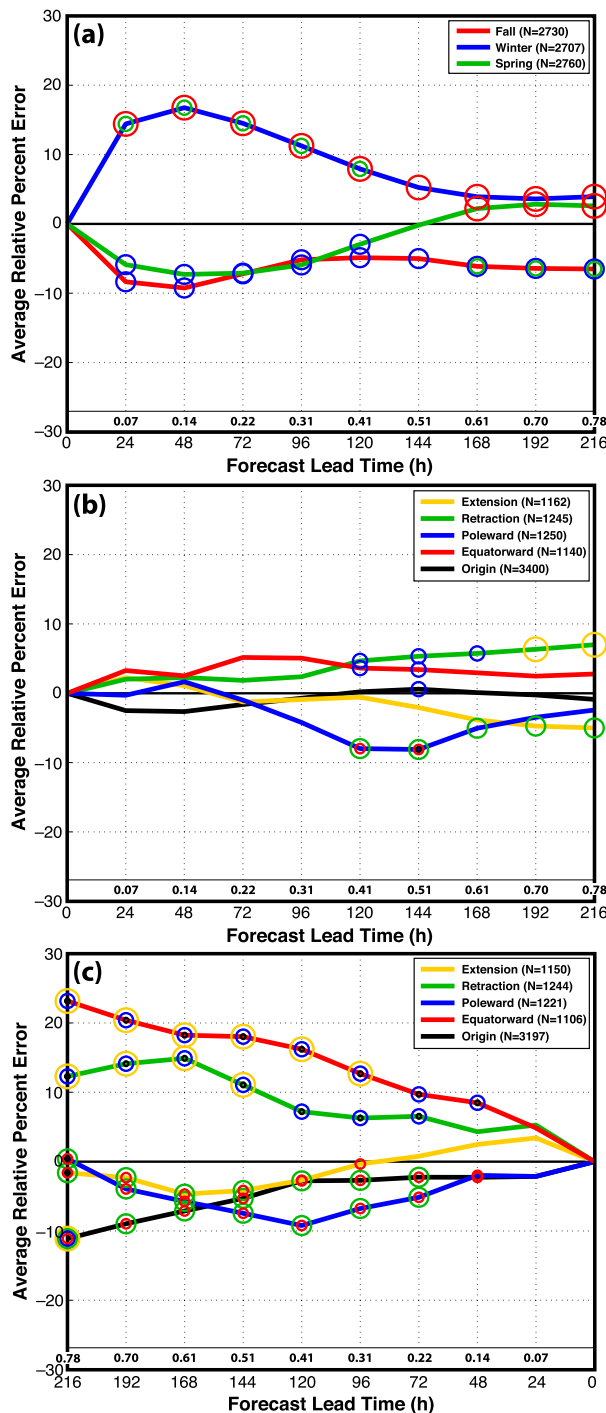


FIG. 8. (a) The average percent distance error of GEFS ensemble mean NPJ phase diagram forecasts initialized during the same season relative to the average distance error of all ensemble mean NPJ phase diagram forecasts initialized during the cool season. Positive (negative) average percent errors correspond to average errors that are greater than (less than) the cool season average. The numbers immediately above the horizontal axis identify the average distance error in standard deviations for all ensemble mean NPJ phase diagram forecasts at a particular lead time. The colored

pattern is considerably more complex than that implied by the NPJ phase diagram. Consequently, the forecast error metric employed in the present study only describes a fraction of the total forecast error insofar as it relates to the position and intensity of the NPJ.

The average distance errors associated with ensemble mean NPJ phase diagram forecasts initialized during the same season are provided in Fig. 8a. The average distance errors are displayed here, and in subsequent figure panels, as an average percent error relative to the average distance error of all ensemble mean NPJ phase diagram forecasts for each lead time. For example, average percent errors greater than (less than) zero indicate that forecasts within a particular category are associated with an average distance error that is greater than (less than) that associated with all ensemble mean NPJ phase diagram forecasts at a certain lead time. At lead times ≤ 120 h, the NPJ phase diagram forecasts initialized during the winter (December–February) exhibit significantly larger distance errors within the NPJ phase diagram than forecasts initialized during the fall (September–November) and spring (March–May). At lead times ≥ 168 h, forecasts initialized during the winter and spring exhibit significantly larger distance errors than forecasts initialized during the fall. Furthermore, forecasts initialized during the fall exhibit distance errors that fall below the cool-season average at all forecast lead times, while forecasts initialized during the winter exhibit errors that lie above the cool-season average at all forecast lead times.

The average distance errors of ensemble mean NPJ phase diagram forecasts initialized during the same NPJ regime are shown in Fig. 8b. At lead times < 120 h, no significant differences in distance error are observed between the NPJ regimes. However, significant differences between the NPJ regimes begin to emerge at lead times ≥ 120 h. Specifically, forecasts initialized during a jet retraction exhibit significantly larger distance errors

←

circles on each line indicate that the error associated with that season is statistically distinct from the error associated with another season at the 99% confidence level (e.g., a red circle on the line corresponding to winter indicates that the error associated with forecasts during the winter is statistically distinct from the error associated with forecasts during the fall at that lead time). The numbers in parentheses in the legend indicate the number of forecasts in that category. Forecast lead time along the horizontal axis represents the hours after forecast initialization. (b) As in (a), but for forecasts initialized during the same NPJ regime. (c) As in (a), but for forecasts verified during the same NPJ regime. Forecast lead time along the horizontal axis in (c) depicts the hours prior to forecast verification.

than forecasts initialized during a poleward shift at lead times between 120 and 168 h, and significantly larger distance errors than forecasts initialized during a jet extension at lead times between 192 and 216 h. However, despite these significant differences at lead times ≥ 120 h, the spread in distance errors between the NPJ regimes is generally small during this time period.

The average distance errors of ensemble mean NPJ phase diagram forecasts verified during the same NPJ regime are shown in Fig. 8c. At lead times ≥ 144 h, forecasts verified during equatorward shifts and jet retractions exhibit significantly larger distance errors than those verified during poleward shifts and jet extensions. Additionally, considerably larger spread between the distance errors associated with each NPJ regime is observed for NPJ phase diagram forecasts verified during the same NPJ regime (Fig. 8c) compared to those initialized during the same NPJ regime (Fig. 8b) for this time period. Consequently, knowledge of the NPJ regime at the time of forecast verification appears to be a greater differentiator of forecast skill with respect to the NPJ phase diagram than knowledge of the NPJ regime at the time of forecast initialization. This result implies that enhanced or reduced confidence can be ascribed to a forecast by considering the forecast evolution of the NPJ with respect to the NPJ phase diagram, rather than by considering the state of the NPJ at the time of forecast initialization.

The poor forecast skill of ensemble mean NPJ phase diagram forecasts verified during equatorward shifts (Fig. 8c) is also apparent when considering the frequency with which each NPJ regime is overforecast or underforecast in the GEFS Reforecast dataset. Figure 9 demonstrates that equatorward shifts are substantially underforecast by ensemble mean NPJ phase diagram forecasts at all lead times compared to the verifying 0-h analyses. Specifically, equatorward shifts are underforecast by nearly 26% at a 216-h lead time, which is at least twice the frequency that the other NPJ regimes are underforecast at the same lead time. While all NPJ regimes are generally underforecast by the ensemble mean NPJ phase diagram forecasts at lead times ≥ 192 h, both jet extensions and poleward shifts are overforecast at lead times ≤ 144 h. The overforecasting of NPJ regimes near the origin of the NPJ phase diagram suggests a general reversion of the ensemble mean 250-hPa zonal wind toward climatology for long forecast lead times.

5. Best and worst NPJ phase diagram forecasts

An examination of the best and worst NPJ phase diagram medium-range forecasts has the potential to illuminate factors that may contribute to enhanced or

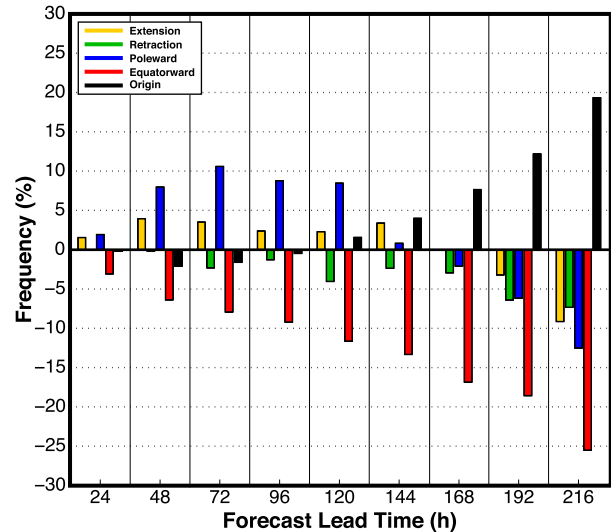


FIG. 9. The percent frequency that an NPJ regime is overforecast or underforecast by the GEFS ensemble mean NPJ phase diagram forecasts relative to the verifying 0-h analyses at each forecast lead time.

reduced forecast skill during the medium-range period (e.g., Lillo and Parsons 2017). The best and worst medium-range forecasts with respect to the NPJ phase diagram are identified in terms of the following two metrics: 1) the magnitude of the GEFS ensemble mean distance error averaged over lead times of 192 and 216 h and 2) the magnitude of the GEFS ensemble member distance error averaged over all ensemble members at lead times of 192 and 216 h. The first metric provides a measure of ensemble-mean forecast accuracy during the medium-range period, while the second metric provides a measure of ensemble-member forecast precision. Those forecasts that rank in the top 10% in terms of the average ensemble mean distance error *and* the top 10% in terms of the average ensemble member distance error are identified as best forecasts. Conversely, those forecasts that rank in the bottom 10% in terms of both metrics (i.e., the largest average distance errors) are identified as worst forecasts.

Figure 10 describes a series of hypothetical NPJ phase diagram forecasts that qualify either as a best, an intermediate, or a worst forecast with respect to the two metrics identified in the previous paragraph. A best forecast (Fig. 10a) is one in which the forecast exhibits a small average ensemble mean distance error and a small average ensemble member distance error. Therefore, a best forecast is interpreted as one in which the forecast is both accurate and precise. An intermediate forecast (Fig. 10b) is one in which there is a small average ensemble mean distance error but also a large average ensemble member distance error. Consequently, the criteria for a best forecast is not met and this situation

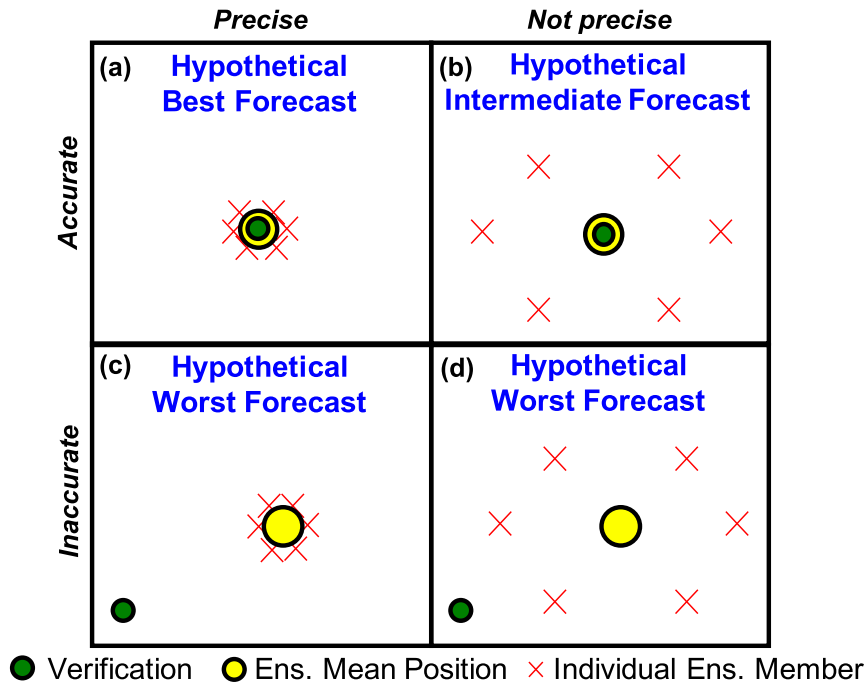


FIG. 10. Schematic illustrating the classification scheme for the best and worst NPJ phase diagram medium-range forecasts. (a),(b) The top row identifies a series of accurate forecasts that vary in their level of precision, while (c),(d) the bottom row identifies a series of inaccurate forecasts that vary in their level of precision.

represents one in which the forecast was accurate but not precise. A worst forecast is one in which there is a large average ensemble mean distance error and a large average ensemble member distance error. Such a forecast can either be inaccurate but precise (Fig. 10c), or inaccurate and not precise (Fig. 10d). Considered together, the worst forecasts can be summarized as those forecasts that feature the highest degree of inaccuracy.

The frequency distribution of the worst NPJ phase diagram forecasts during the cool season features two separate maxima during December and during February–April, while the best NPJ phase diagram forecasts occur most frequently during September (Fig. 11a). The best and worst NPJ phase diagram forecasts are classified based on the NPJ regime at the time of forecast initialization in Fig. 11b. This frequency distribution indicates that the worst forecasts are initialized disproportionately more than the best forecasts during jet retractions and equatorward shifts, while the best forecasts are initialized disproportionately more than the worst forecasts during jet extensions and poleward shifts. The average values of PC 1 and PC 2 at the time of forecast initialization (Table 2) also indicate a preference for the worst forecasts to be initialized most frequently during jet retractions and equatorward shifts, and for the best forecasts to be initialized most frequently during jet

extensions and poleward shifts. However, only the values of PC 1 are significantly different between the best and worst forecasts at the time of forecast initialization.

The evolution of the NPJ during the 10-day period following the initialization of a best and worst NPJ phase diagram forecast also differs considerably (Table 2). In particular, the average change in PC 2 ($\Delta PC 2$) during the 10-day period following the initialization of a worst forecast indicates a significant movement of the NPJ toward an equatorward shift within the NPJ phase diagram, while the $\Delta PC 2$ following the initialization of a best forecast indicates a significant movement of the NPJ toward a poleward shift. Additionally, the worst forecast periods feature significantly longer trajectories within the NPJ phase diagram compared to the best forecast periods during the 10-day period following forecast initialization (Table 2). As will be demonstrated, this result is consistent with the notion that the worst forecasts often occur during periods characterized by rapid NPJ regime change, while the best forecast periods are often characterized by more persistent upper-tropospheric flow patterns over the North Pacific in comparison. This notion aligns well with previous work suggesting that periods characterized by upper-tropospheric regime change are generally associated with reduced forecast skill (e.g., Tibaldi and Molteni 1990; Frederiksen et al. 2004;

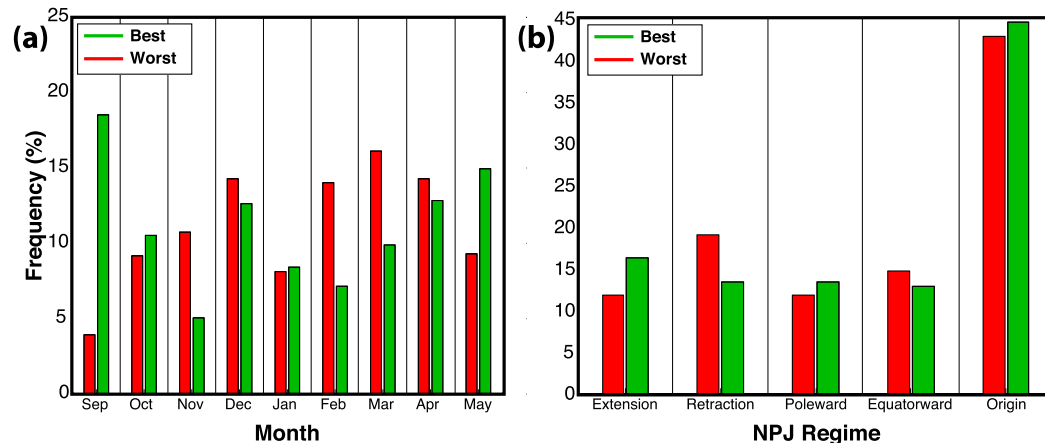


FIG. 11. (a) The percent frequency of the best and worst NPJ phase diagram medium-range forecasts that are initialized during each month of the cool season. (b) The percent frequency of the best and worst NPJ phase diagram medium-range forecasts that are initialized during each NPJ regime.

Pelly and Hoskins 2003; Ferranti et al. 2015; Lillo and Parsons 2017).

An examination of the upper-tropospheric flow patterns associated with the best and worst forecast periods offers insight into the types of large-scale flow patterns that are characterized by enhanced or reduced forecast skill. This examination is performed by employing the CFSR to construct composite analyses of 250-hPa wind speed, geopotential height, and geopotential height anomalies at the time a best and a worst forecast are initialized, as well as at 192 h following forecast initialization. Two-sided Student's t tests are used to evaluate whether the differences between geopotential height anomalies associated with the worst and best forecast composites are statistically significant at the 99% confidence level at each time period.

The composite upper-tropospheric flow patterns at the time a best and a worst forecast are initialized within each NPJ regime are provided in Fig. 12. At first glance, an examination of the geopotential height anomalies in Fig. 12 reveals minor qualitative differences between the best and worst forecasts that are initialized during the

same NPJ regime. However, a calculation of the difference between geopotential height anomalies associated with the worst and best forecasts reveals some significant features (Fig. 13). In particular, while both the best and worst forecasts that are initialized during a jet extension exhibit a strong, zonally extended NPJ at the time of forecast initialization (Figs. 12a,b), the worst forecasts are characterized by significantly higher geopotential height anomalies over the eastern North Pacific compared to the best forecasts (Fig. 13a). Similarly, while both the best and worst forecasts that are initialized during a jet retraction feature an anomalous ridge over the central North Pacific (Figs. 12c,d), the worst forecasts also exhibit significantly higher geopotential height anomalies over the eastern North Pacific compared to the best forecasts (Fig. 13b). The worst forecasts that are initialized during a jet retraction also feature significantly lower geopotential height anomalies over the subtropical North Pacific and the western Great Lakes compared to the best forecasts (Fig. 13b).

Similar to jet extensions and jet retractions, the worst forecasts that are initialized during a poleward shift

TABLE 2. NPJ phase diagram characteristics derived from the CFSR for the periods characterized by the best and worst NPJ phase diagram medium-range forecasts with all quantities expressed in standard deviations. Terms Δ PC 1 and Δ PC 2 represent the change in PC 1 and PC 2, respectively, during the 10-day period following the initialization of a best and a worst forecast. Positive (negative) values for Δ PC 1 and Δ PC 2 represent an NPJ that undergoes a jet extension and poleward shift (jet retraction and equatorward shift), respectively. The average 10-day trajectory length corresponds to the average Euclidean distance traveled by the NPJ within the NPJ phase diagram during the 10-day period following the initialization of a best and a worst forecast. Shorter trajectories correspond to a more persistent NPJ configuration compared to longer trajectories.

	Avg start PC 1	Avg start PC 2	Avg 10-day Δ PC 1	Avg 10-day Δ PC 2	Avg 10-day trajectory length
Best forecasts ($N = 475$)	0.09 ^a	0.04	0.09	0.16 ^a	3.50 ^a
Worst forecasts ($N = 763$)	-0.18 ^a	-0.08	0.01	-0.21 ^a	4.33 ^a

^a Values associated with the best and worst forecasts are statistically significantly different at the 99.9% confidence level.

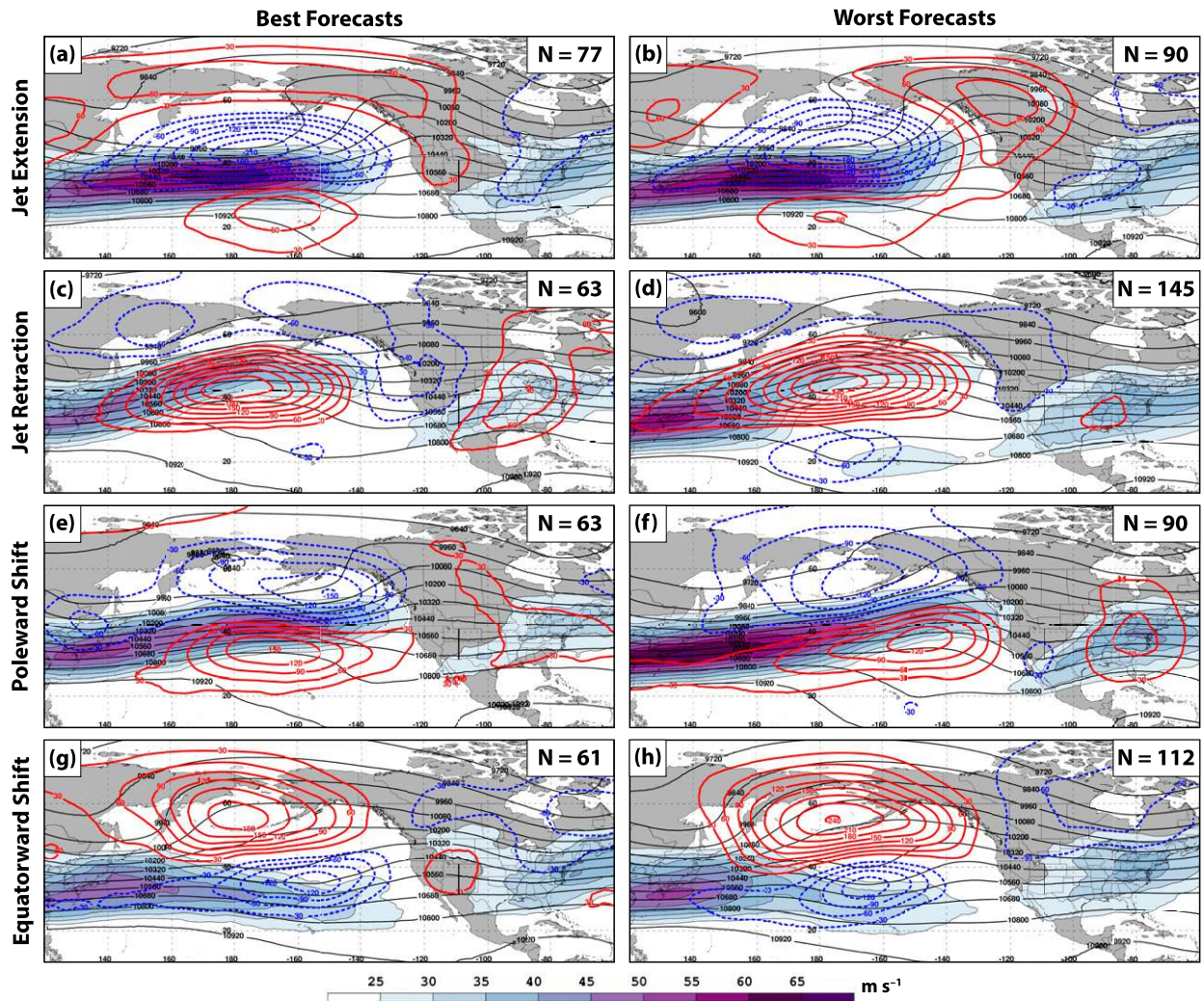


FIG. 12. Composite mean 250-hPa wind speed (m s^{-1}) is shaded in the fill pattern, 250-hPa geopotential height is contoured in black every 120 m, and 250-hPa geopotential height anomalies are contoured in solid red and dashed blue every 30 m for positive and negative values, respectively, at the time (a) a best and (b) a worst NPJ phase diagram forecast is initialized during a jet extension. (c),(d) As in (a),(b), but for those forecasts that are initialized during a jet retraction. (e),(f) As in (a),(b), but for those forecasts that are initialized during a poleward shift. (g),(h) As in (a),(b), but for those forecasts that are initialized during an equatorward shift. The quantities in the top-right corner of every panel indicate the number of cases included in each composite.

exhibit significantly higher geopotential height anomalies over the eastern North Pacific compared to the best forecasts (Figs. 12e,f and 13c). Furthermore, the worst forecasts that are initialized during a poleward shift feature a more intense NPJ, a stronger jet stream over North America, and significantly lower geopotential height anomalies over the southwestern United States and northwestern Mexico compared to the best forecasts (Figs. 12e,f and 13c). While not as large in magnitude compared to the other composites, the worst forecasts that are initialized during an equatorward shift also exhibit significantly higher geopotential height anomalies over the eastern North Pacific compared to the best

forecasts (Figs. 12g,h and 13d). Consequently, the presence of higher geopotential height anomalies over the eastern North Pacific at the time of forecast initialization is a distinguishing factor between the worst and best forecasts regardless of the prevailing NPJ regime.

Substantial differences in the upper-tropospheric flow pattern over the North Pacific are observed 192 h following the initialization of a best and a worst forecast. In particular, the upper-tropospheric flow pattern 192 h following the initialization of a best forecast is characterized by the meridional juxtaposition of an anomalous trough and an anomalous ridge over the central North Pacific regardless of the NPJ regime at the time of

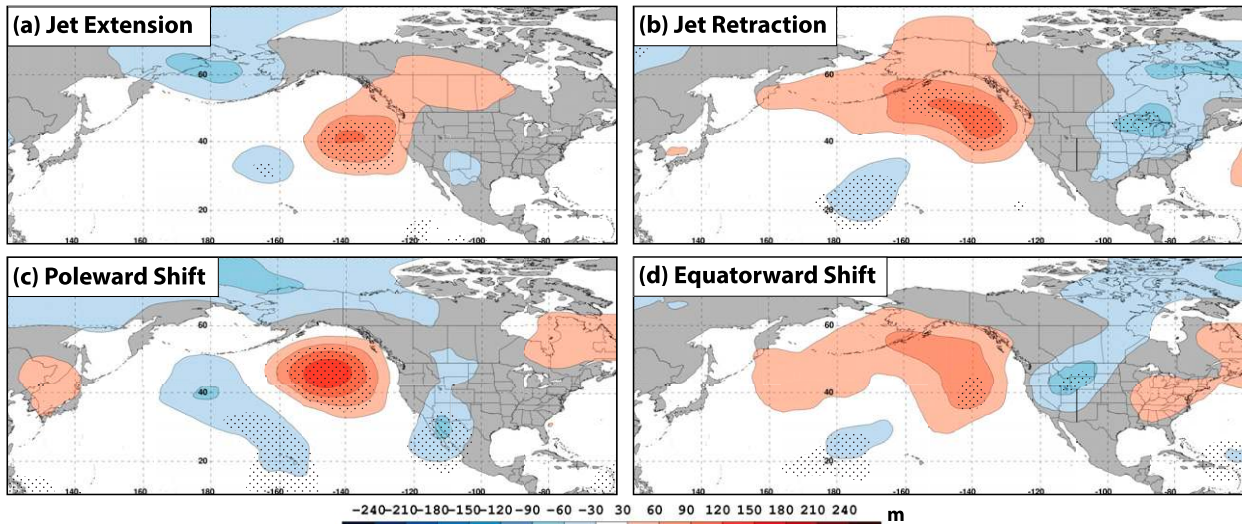


FIG. 13. (a) The difference between the 250-hPa geopotential height anomalies associated with a worst and a best NPJ phase diagram forecast at the time of forecast initialization during a jet extension is shaded every 30 m in the fill pattern. (b) As in (a), but during a jet retraction. (c) As in (a), but during a poleward shift. (d) As in (a), but during an equatorward shift. Statistically significant differences in geopotential height anomalies at the 99% confidence level are stippled in all panels.

forecast initialization (Figs. 14a,c,e,g). This pattern subsequently favors an NPJ that is extended and poleward shifted in the best forecast composites relative to the worst forecast composites. Downstream of the anomalous trough over the North Pacific, an anomalous ridge is also firmly positioned over North America in the best forecast composites. In contrast to the best forecasts, the upper-tropospheric flow pattern 192 h following the initialization of a worst forecast features an anomalous ridge over the high-latitude North Pacific and a retracted NPJ regardless of the NPJ regime at the time of forecast initialization (Figs. 14b,d,f,h). An anomalous trough of variable strength is also located over North America in all of the worst forecast composites.

The difference between the geopotential height anomalies 192 h following the initialization of a worst and a best forecast is shown in Fig. 15. Compared to the best forecast composites, all of the worst forecast composites exhibit significantly higher geopotential height anomalies over the high-latitude North Pacific, and significantly lower geopotential height anomalies over the subtropical North Pacific (Figs. 15a–d), reminiscent of a Rex block (Rex 1950). Notably, this difference pattern prevails regardless of the NPJ regime at the time of forecast initialization. Consequently, the upper-tropospheric flow patterns shown in Fig. 15 uniformly suggest that periods characterized by the development and/or maintenance of upper-tropospheric blocking events over the North Pacific are associated with reduced forecast skill with respect to the NPJ phase diagram. Conversely, reversing the sign of the difference field in

Fig. 15 (not shown) suggests that periods evolving toward a zonal NPJ over the North Pacific are generally associated with enhanced forecast skill.

6. Discussion and conclusions

The preceding analysis corroborates the results from prior studies on NPJ variability that establish a relationship between the two leading modes of 250-hPa zonal wind variability over the North Pacific and the large-scale flow pattern over North America (e.g., Athanasiadis et al. 2010; Jaffe et al. 2011; Griffin and Martin 2017). Provided with this relationship, this study utilizes the two leading modes of 250-hPa zonal wind variability within the CFSR during the cool season as the foundation for developing an NPJ phase diagram. The NPJ phase diagram subsequently provides an objective tool to monitor the state and evolution of the upper-tropospheric flow pattern over the North Pacific, to identify the prevailing NPJ regime, and to evaluate the characteristic forecast skill associated with each NPJ regime.

The application of the NPJ phase diagram to 250-hPa zonal wind data from the CFSR during 1979–2014 excluding the summer months reveals several salient characteristics of each NPJ regime and highlights opportunities for additional research. For example, while the mean and median residence times within a particular NPJ regime are typically on the order of 3 days, an NPJ regime can persist for multiple weeks. Furthermore, it is apparent that the frequency of each NPJ regime is

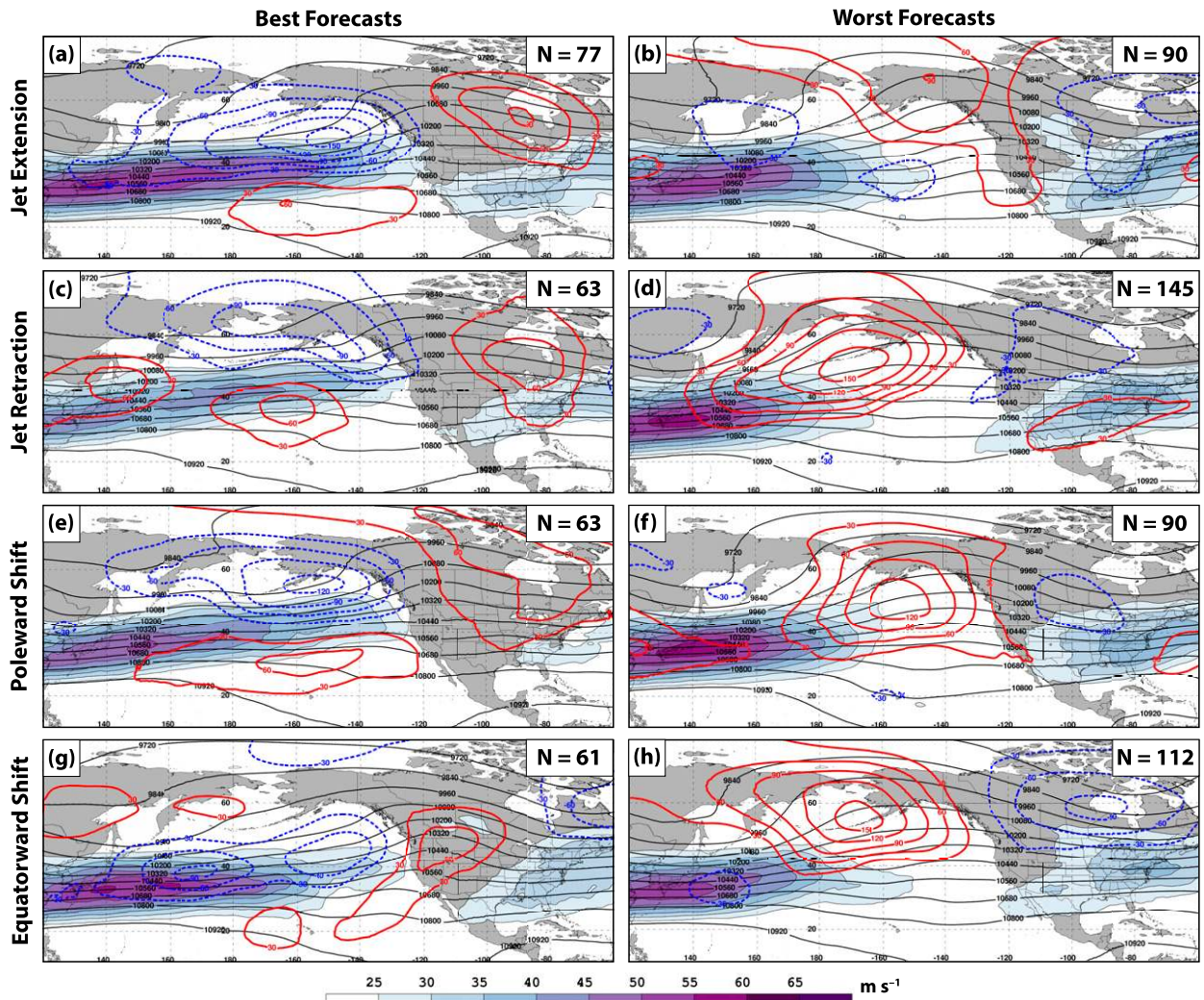


FIG. 14. As in Fig. 12, but for the composite 250-hPa flow patterns 192 h following the initialization of a best and a worst NPJ phase diagram forecast.

characterized by considerable interannual and intra-seasonal variability. Given that each NPJ regime can strongly influence the character of the downstream flow pattern over North America, further investigation into the types of large-scale flow patterns that are conducive to prolonged residence times within an NPJ regime, or that increase the frequency of an NPJ regime, may add considerable value to operational seasonal and sub-seasonal forecasts over North America.

Large-scale atmospheric teleconnection patterns, such as the PNA, AO, and ENSO, are strongly related to the frequency of each NPJ regime. For example, it was noted that a positive (negative) PNA is most frequently characterized by jet extensions and poleward shifts (jet retractions and equatorward shifts). Jet extensions and poleward shifts are associated with different lower-tropospheric temperature anomaly patterns over North

America, however, with jet extensions favoring anomalously cold temperatures over eastern North America and poleward shifts favoring anomalously warm temperatures over northern North America. Consequently, knowledge of the prevailing NPJ regime in combination with the phase of the PNA index provides additional value to operational forecasts of temperature over North America.

The NPJ phase diagram provides an objective basis for detailed investigations of NPJ variability during other well-established atmospheric teleconnection patterns, as well, such as the North Atlantic Oscillation (e.g., Wallace and Gutzler 1981) and the Madden–Julian oscillation (Madden and Julian 1972). Such investigations have the potential to identify the variety of large-scale flow evolutions over the North Pacific that occur during a particular atmospheric teleconnection pattern. Similar to the approach utilized by Madonna et al. (2017) in their

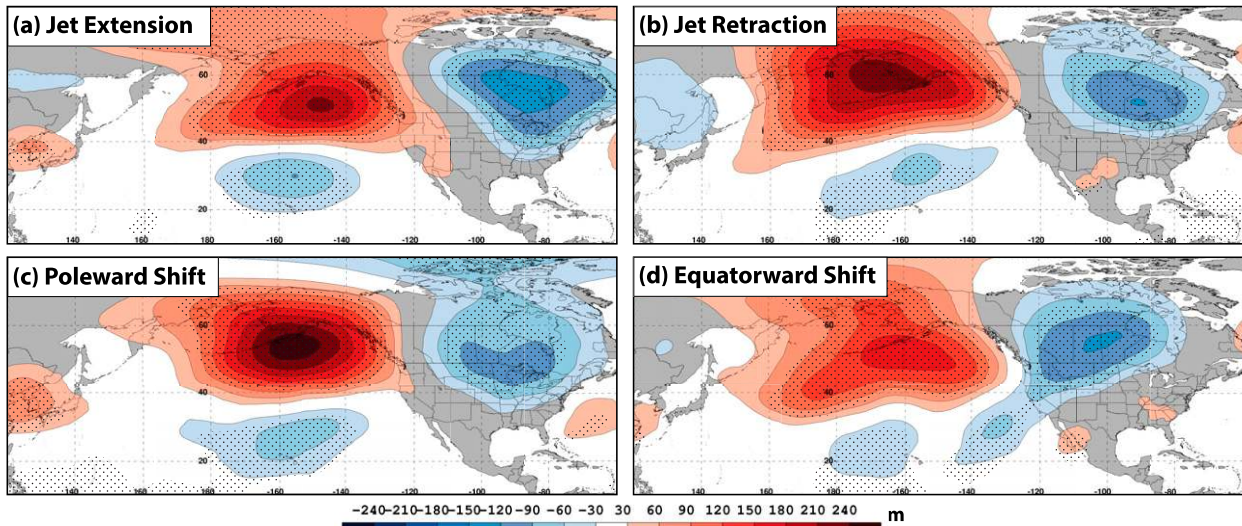


FIG. 15. As in Fig. 13, but for the composite difference between 250-hPa geopotential height anomalies 192 h following the initialization of a worst and a best NPJ phase diagram forecast.

investigation of North Atlantic jet variability, cluster analysis techniques can also be applied to 250-hPa zonal wind data to identify recurring nonlinear configurations of the NPJ. These recurring nonlinear configurations of the NPJ can be subsequently paired with the results from the present study to provide a complementary perspective on NPJ variability.

An examination of the forecast skill associated with each NPJ regime reveals the types of large-scale flow patterns that exhibit reduced forecast skill with respect to the NPJ phase diagram. In particular, the analysis suggests that forecasts verified during jet retractions and equatorward shifts exhibit significantly reduced forecast skill compared to jet extensions and poleward shifts at lead times ≥ 144 h. Recall that both jet retractions and equatorward shifts are typically characterized by an anomalous upper-tropospheric ridge in the central North Pacific. In light of these two observations, and given that diabatic processes can play an important role in amplifying the upper-tropospheric flow pattern (e.g., Massacand et al. 2001; Riemer et al. 2008; Torn 2010; Ferranti et al. 2015; Pfahl et al. 2015; Grams and Archambault 2016; Bosart et al. 2017), it is hypothesized that diabatic processes account for a considerable fraction of the reduced forecast skill associated with jet retractions and equatorward shifts. Additional case study work that utilizes the NPJ phase diagram to investigate poor forecasts verified during jet retractions and equatorward shifts is likely to determine the degree to which diabatic processes contribute to the reduced forecast skill associated with these NPJ regimes.

An analysis of the best and worst medium-range forecasts with respect to the NPJ phase diagram

suggests that the worst forecasts are often associated with the development and/or maintenance of upper-tropospheric blocking events over the North Pacific. This result aligns well with previous work highlighting the reduced predictability associated with the development and/or maintenance of blocking events (e.g., Tibaldi and Molteni 1990; D'Andrea et al. 1998; Frederiksen et al. 2004; Pelly and Hoskins 2003; Matsueda 2011; Ferranti et al. 2015) and holds regardless of the prevailing NPJ regime at the time of forecast initialization. Given this variability in the prevailing NPJ regime prior to blocking events, additional work is required to determine the types of large-scale flow evolutions that are most conducive to block development. The NPJ phase diagram is well suited for such work by providing an objective frame of reference from which to examine the spectrum of large-scale flow evolutions that are conducive to block development. The analysis also indicates that the worst forecast periods are associated with a significant movement of the NPJ toward an equatorward shift within the NPJ phase diagram during the 10-day period following forecast initialization, while the best forecast periods are associated with a significant movement of the NPJ toward a poleward shift. Given that certain trajectories within the NPJ phase diagram are associated with reduced forecast skill, the NPJ phase diagram represents a tool that can be used to objectively identify NPJ regime transitions and to isolate the characteristic large-scale flow patterns associated with those regime transitions. The results from such an investigation have the potential to add considerable value to operational forecasts during periods of regime transition.

The relative forecast skill associated with each NPJ regime is only applicable with respect to the GEFS Reforecast dataset in the present study. Consequently, additional research is required to evaluate the forecast skill of NPJ regimes with respect to other ensemble prediction systems (EPSs). An evaluation of forecast skill with respect to other EPSs has the potential to determine whether the large-scale flow patterns that exhibit reduced skill in the GEFS Reforecast dataset differ from those that exhibit reduced skill in other EPSs. To the degree that differences exist in the forecast skill of each NPJ regime across EPSs, such an evaluation has the potential to identify situations during which greater confidence can be ascribed to a particular EPS and to identify systematic biases in the evolution of certain large-scale flow patterns over the North Pacific.

Acknowledgments. The authors thank Mike Bodner, Daniel Halperin, Arlene Laing, Bill Lamberson, Sara Ganetis, and Josh Kastman for their constructive discussions concerning the NPJ phase diagram. The authors also thank three anonymous reviewers for their constructive comments on this work and the National Oceanic and Atmospheric Administration for its support of this work via Grant NA15NWS4680006.

REFERENCES

- Archambault, H. M., L. F. Bosart, D. Keyser, and J. M. Cordeira, 2013: A climatological analysis of the extratropical flow response to recurring western North Pacific tropical cyclones. *Mon. Wea. Rev.*, **141**, 2325–2346, <https://doi.org/10.1175/MWR-D-12-00257.1>.
- , D. Keyser, L. F. Bosart, C. A. Davis, and J. M. Cordeira, 2015: A composite perspective of the extratropical flow response to recurring western North Pacific tropical cyclones. *Mon. Wea. Rev.*, **143**, 1122–1141, <https://doi.org/10.1175/MWR-D-14-00270.1>.
- Athanasiadis, P. J., J. M. Wallace, and J. J. Wettstein, 2010: Patterns of wintertime jet stream variability and their relation to the storm tracks. *J. Atmos. Sci.*, **67**, 1361–1381, <https://doi.org/10.1175/2009JAS3270.1>.
- Barnston, A. G., and R. E. Livezey, 1987: Classification, seasonality and persistence of low-frequency atmospheric circulation patterns. *Mon. Wea. Rev.*, **115**, 1083–1126, [https://doi.org/10.1175/1520-0493\(1987\)115<1083:CSAPOL>2.0.CO;2](https://doi.org/10.1175/1520-0493(1987)115<1083:CSAPOL>2.0.CO;2).
- Bosart, L. F., B. J. Moore, J. M. Cordeira, and H. M. Archambault, 2017: Interactions of North Pacific tropical, midlatitude, and polar disturbances resulting in linked extreme weather events over North America in October 2007. *Mon. Wea. Rev.*, **145**, 1245–1273, <https://doi.org/10.1175/MWR-D-16-0230.1>.
- Chang, E. K. M., S. Lee, and K. L. Swanson, 2002: Storm track dynamics. *J. Climate*, **15**, 2163–2183, [https://doi.org/10.1175/1520-0442\(2002\)015<02163:STD>2.0.CO;2](https://doi.org/10.1175/1520-0442(2002)015<02163:STD>2.0.CO;2).
- Cook, A. R., L. M. Leslie, D. B. Parsons, and J. T. Schaefer, 2017: The impact of El Niño–Southern Oscillation (ENSO) on winter and early spring U.S. tornado outbreaks. *J. Appl. Meteor. Climatol.*, **56**, 2455–2478, <https://doi.org/10.1175/JAMC-D-16-0249.1>.
- CPC, 2017a: Arctic Oscillation. Climate Prediction Center, http://www.cpc.ncep.noaa.gov/products/precip/CWlink/daily_ao_index/ao.shtml.
- , 2017b: Pacific/North American pattern. Climate Prediction Center, <http://www.cpc.ncep.noaa.gov/products/precip/CWlink/pna/pna.shtml>.
- D’Andrea, F., and Coauthors, 1998: Northern Hemisphere atmospheric blocking as simulated by 15 atmospheric general circulation models in the period 1979–1988. *Climate Dyn.*, **14**, 385–407, <https://doi.org/10.1007/s003820050230>.
- Eichelberger, S. J., and D. L. Hartmann, 2007: Zonal jet structure and the leading mode of variability. *J. Climate*, **20**, 5149–5163, <https://doi.org/10.1175/JCLI4279.1>.
- ESRL, 2017: Niño 3.4 SST index. Earth System Research Laboratory, https://www.esrl.noaa.gov/psd/gcos_wgsp/Timeseries/Nino34/.
- Ferranti, L., S. Corti, and M. Janousek, 2015: Flow-dependent verification of the ECMWF ensemble over the Euro-Atlantic sector. *Quart. J. Roy. Meteor. Soc.*, **141**, 916–924, <https://doi.org/10.1002/qj.2411>.
- Franzke, C., and S. B. Feldstein, 2005: The continuum and dynamics of Northern Hemisphere teleconnection patterns. *J. Atmos. Sci.*, **62**, 3250–3267, <https://doi.org/10.1175/JAS3536.1>.
- , —, and S. Lee, 2011: Synoptic analysis of the Pacific–North American teleconnection pattern. *Quart. J. Roy. Meteor. Soc.*, **137**, 329–346, <https://doi.org/10.1002/qj.768>.
- Frederiksen, J. S., M. A. Collier, and A. B. Watkins, 2004: Ensemble prediction of blocking regime transitions. *Tellus*, **56A**, 485–500, <https://doi.org/10.1111/j.1600-0870.2004.00075.x>.
- Grams, C. M., and H. M. Archambault, 2016: The key role of diabatic outflow in amplifying the midlatitude flow: A representative case study of weather systems surrounding western North Pacific extratropical transition. *Mon. Wea. Rev.*, **144**, 3847–3869, <https://doi.org/10.1175/MWR-D-15-0419.1>.
- Griffin, K. S., and J. E. Martin, 2017: Synoptic features associated with temporally coherent modes of variability of the North Pacific jet stream. *J. Climate*, **30**, 39–54, <https://doi.org/10.1175/JCLI-D-15-0833.1>.
- Hakim, G. J., 2003: Developing wave packets in the North Pacific storm track. *Mon. Wea. Rev.*, **131**, 2824–2837, [https://doi.org/10.1175/1520-0493\(2003\)131<2824:DWPITN>2.0.CO;2](https://doi.org/10.1175/1520-0493(2003)131<2824:DWPITN>2.0.CO;2).
- Hamill, T. M., G. T. Bates, J. S. Whitaker, D. R. Murray, M. Fiorino, T. J. Galarneau Jr., Y. Zhu, and W. Lapenta, 2013: NOAA’s second-generation global medium-range ensemble reforecast dataset. *Bull. Amer. Meteor. Soc.*, **94**, 1553–1565, <https://doi.org/10.1175/BAMS-D-12-00014.1>.
- Handlos, Z. J., and J. E. Martin, 2016: Composite analysis of large-scale environments conducive to western Pacific polar/subtropical jet superposition. *J. Climate*, **29**, 7145–7165, <https://doi.org/10.1175/JCLI-D-16-0044.1>.
- Harr, P. A., and J. M. Dea, 2009: Downstream development associated with the extratropical transition of tropical cyclones over the western North Pacific. *Mon. Wea. Rev.*, **137**, 1295–1319, <https://doi.org/10.1175/2008MWR2558.1>.
- Higgins, R. W., J.-K. E. Schemm, W. Shi, and A. Leetmaa, 2000: Extreme precipitation events in the western United States related to tropical forcing. *J. Climate*, **13**, 793–820, [https://doi.org/10.1175/1520-0442\(2000\)013<0793:EPEITW>2.0.CO;2](https://doi.org/10.1175/1520-0442(2000)013<0793:EPEITW>2.0.CO;2).
- Horel, J. D., and J. M. Wallace, 1981: Planetary-scale atmospheric phenomena associated with the Southern Oscillation. *Mon. Wea. Rev.*, **109**, 813–829, [https://doi.org/10.1175/1520-0493\(1981\)109<0813:PSAPAW>2.0.CO;2](https://doi.org/10.1175/1520-0493(1981)109<0813:PSAPAW>2.0.CO;2).
- Hoskins, B. J., and D. J. Karoly, 1981: The steady linear response of a spherical atmosphere to thermal and orographic forcing.

- J. Atmos. Sci.*, **38**, 1179–1196, [https://doi.org/10.1175/1520-0469\(1981\)038<1179:TSLROA>2.0.CO;2](https://doi.org/10.1175/1520-0469(1981)038<1179:TSLROA>2.0.CO;2).
- Jaffe, S. C., J. E. Martin, D. J. Vimont, and D. J. Lorenz, 2011: A synoptic climatology of episodic, subseasonal retractions of the Pacific jet. *J. Climate*, **24**, 2846–2860, <https://doi.org/10.1175/2010JCLI3995.1>.
- Jhun, J.-G., and E.-J. Lee, 2004: A new East Asian winter monsoon index and associated characteristics of the winter monsoon. *J. Climate*, **17**, 711–726, [https://doi.org/10.1175/1520-0442\(2004\)017<0711:ANEAWM>2.0.CO;2](https://doi.org/10.1175/1520-0442(2004)017<0711:ANEAWM>2.0.CO;2).
- Kalnay, E., and Coauthors, 1996: The NCEP/NCAR 40-Year Reanalysis Project. *Bull. Amer. Meteor. Soc.*, **77**, 437–471, [https://doi.org/10.1175/1520-0477\(1996\)077<0437:TNYRP>2.0.CO;2](https://doi.org/10.1175/1520-0477(1996)077<0437:TNYRP>2.0.CO;2).
- Lee, Y.-Y., G.-H. Lim, and J.-S. Kug, 2010: Influence of the East Asian winter monsoon on the storm track activity over the North Pacific. *J. Geophys. Res.*, **115**, D09102, <https://doi.org/10.1029/2009JD012812>.
- Li, C., and J. J. Wettstein, 2012: Thermally driven and eddy-driven jet variability in reanalysis. *J. Climate*, **25**, 1587–1596, <https://doi.org/10.1175/JCLI-D-11-00145.1>.
- Lillo, S. P., and D. B. Parsons, 2017: Investigating the dynamics of error growth in ECMWF medium-range forecast busts. *Quart. J. Roy. Meteor. Soc.*, **143**, 1211–1226, <https://doi.org/10.1002/qj.2938>.
- Lin, H., and J. Derome, 1996: Changes in predictability associated with the PNA pattern. *Tellus*, **48A**, 553–571, <https://doi.org/10.3402/tellusa.v48i4.12139>.
- Madden, R. A., and P. R. Julian, 1972: Description of global-scale circulation cells in the tropics with a 40–50 day period. *J. Atmos. Sci.*, **29**, 1109–1123, [https://doi.org/10.1175/1520-0469\(1972\)029<1109:DOGSCC>2.0.CO;2](https://doi.org/10.1175/1520-0469(1972)029<1109:DOGSCC>2.0.CO;2).
- , and —, 1994: Observations of the 40–50-day tropical oscillation—A review. *Mon. Wea. Rev.*, **122**, 814–837, [https://doi.org/10.1175/1520-0493\(1994\)122<0814:OOTDFO>2.0.CO;2](https://doi.org/10.1175/1520-0493(1994)122<0814:OOTDFO>2.0.CO;2).
- Madonna, E., C. Li, C. M. Grams, and T. Woollings, 2017: The link between eddy-driven jet variability and weather regimes in the North Atlantic-European sector. *Quart. J. Roy. Meteor. Soc.*, **143**, 2960–2972, <https://doi.org/10.1002/qj.3155>.
- Massacand, A. C., H. Wernli, and H. C. Davies, 2001: Influence of upstream diabatic heating upon an alpine event of heavy precipitation. *Mon. Wea. Rev.*, **129**, 2822–2828, [https://doi.org/10.1175/1520-0493\(2001\)129<2822:IOUDHU>2.0.CO;2](https://doi.org/10.1175/1520-0493(2001)129<2822:IOUDHU>2.0.CO;2).
- Matsueda, M., 2011: Predictability of Euro-Russian blocking in summer of 2010. *Geophys. Res. Lett.*, **38**, L06801, <https://doi.org/10.1029/2010GL046557>.
- North, G. R., T. L. Bell, R. F. Cahalan, and F. J. Moeng, 1982: Sampling errors in the estimation of empirical orthogonal functions. *Mon. Wea. Rev.*, **110**, 699–706, [https://doi.org/10.1175/1520-0493\(1982\)110<0699:SEITEO>2.0.CO;2](https://doi.org/10.1175/1520-0493(1982)110<0699:SEITEO>2.0.CO;2).
- Orlanski, I., and J. P. Sheldon, 1995: Stages in the energetics of baroclinic systems. *Tellus*, **47A**, 605–628, <https://doi.org/10.3402/tellusa.v47i5.11553>.
- Palmer, T. N., 1988: Medium and extended range predictability and stability of the Pacific/North American mode. *Quart. J. Roy. Meteor. Soc.*, **114**, 691–713, <https://doi.org/10.1002/qj.49711448108>.
- Pelly, J. L., and B. J. Hoskins, 2003: How well does the ECMWF Ensemble Prediction System predict blocking? *Quart. J. Roy. Meteor. Soc.*, **129**, 1683–1702, <https://doi.org/10.1256/jq.01.173>.
- Pfahl, S., C. Schwierz, M. Croci-Maspoli, C. M. Grams, and H. Wernli, 2015: Importance of latent heat release in ascending air streams for atmospheric blocking. *Nat. Geosci.*, **8**, 610–614, <https://doi.org/10.1038/ngeo2487>.
- Rasmusson, E. M., and J. M. Wallace, 1983: Meteorological aspects of the El Niño/Southern Oscillation. *Science*, **222**, 1195–1202, <https://doi.org/10.1126/science.222.4629.1195>.
- , and K. Mo, 1993: Linkages between 200-mb tropical and extratropical circulation anomalies during the 1986–1989 ENSO cycle. *J. Climate*, **6**, 595–616, [https://doi.org/10.1175/1520-0442\(1993\)006<0595:LBMTAE>2.0.CO;2](https://doi.org/10.1175/1520-0442(1993)006<0595:LBMTAE>2.0.CO;2).
- Rex, D. F., 1950: Blocking action in the middle troposphere and its effect upon regional climate. I: An aerological study of blocking action. *Tellus*, **2**, 196–211, <https://doi.org/10.1111/j.2153-3490.1950.tb00331.x>.
- Riemer, M., S. C. Jones, and C. A. Davis, 2008: The impact of extratropical transition on the downstream flow: An idealized modelling study with a straight jet. *Quart. J. Roy. Meteor. Soc.*, **134**, 69–91, <https://doi.org/10.1002/qj.189>.
- Saha, S., and Coauthors, 2010: The NCEP Climate Forecast System Reanalysis. *Bull. Amer. Meteor. Soc.*, **91**, 1015–1057, <https://doi.org/10.1175/2010BAMS3001.1>.
- , and Coauthors, 2014: The NCEP Climate Forecast System version 2. *J. Climate*, **27**, 2185–2208, <https://doi.org/10.1175/JCLI-D-12-00823.1>.
- Schubert, S. D., and C.-K. Park, 1991: Low-frequency intraseasonal tropical–extratropical interactions. *J. Atmos. Sci.*, **48**, 629–650, [https://doi.org/10.1175/1520-0469\(1991\)048<0629:LFITEI>2.0.CO;2](https://doi.org/10.1175/1520-0469(1991)048<0629:LFITEI>2.0.CO;2).
- Sheng, J., 2002: GCM experiments on changes in atmospheric predictability associated with the PNA pattern and tropical SST anomalies. *Tellus*, **54A**, 317–329, <https://doi.org/10.1034/j.1600-0870.2002.01324.x>.
- Strong, C., and R. E. Davis, 2008: Variability in the position and strength of winter jet stream cores related to Northern Hemisphere teleconnections. *J. Climate*, **21**, 584–592, <https://doi.org/10.1175/2007JCLI1723.1>.
- Thompson, D. W. J., and J. M. Wallace, 1998: The Arctic oscillation signature in wintertime geopotential height and temperature fields. *Geophys. Res. Lett.*, **25**, 1297–1300, <https://doi.org/10.1029/98GL00950>.
- Tibaldi, S., and F. Molteni, 1990: On the operational predictability of blocking. *Tellus*, **42A**, 343–365, <https://doi.org/10.3402/tellusa.v42i3.11882>.
- Torn, R. D., 2010: Diagnosis of the downstream ridging associated with extratropical transition using short-term ensemble forecasts. *J. Atmos. Sci.*, **67**, 817–833, <https://doi.org/10.1175/2009JAS3093.1>.
- , and G. J. Hakim, 2015: Comparison of wave packets associated with extratropical transition and winter cyclones. *Mon. Wea. Rev.*, **143**, 1782–1803, <https://doi.org/10.1175/MWR-D-14-00006.1>.
- Wallace, J. M., and D. S. Gutzler, 1981: Teleconnections in the geopotential height field during the Northern Hemisphere winter. *Mon. Wea. Rev.*, **109**, 784–812, [https://doi.org/10.1175/1520-0493\(1981\)109<0784:TITGHF>2.0.CO;2](https://doi.org/10.1175/1520-0493(1981)109<0784:TITGHF>2.0.CO;2).
- Wang, L., and W. Chen, 2014: An intensity index for the East Asian winter monsoon. *J. Climate*, **27**, 2361–2374, <https://doi.org/10.1175/JCLI-D-13-00086.1>.
- Weare, B. C., and J. S. Nasstrom, 1982: Examples of extended empirical orthogonal function analyses. *Mon. Wea. Rev.*, **110**, 481–485, [https://doi.org/10.1175/1520-0493\(1982\)110<0481:EOEOF>2.0.CO;2](https://doi.org/10.1175/1520-0493(1982)110<0481:EOEOF>2.0.CO;2).
- Wettstein, J. J., and J. M. Wallace, 2010: Observed patterns of month-to-month storm-track variability and their relationship

- to the background flow. *J. Atmos. Sci.*, **67**, 1420–1437, <https://doi.org/10.1175/2009JAS3194.1>.
- Wilks, D. S., 2011: *Statistical Methods in the Atmospheric Sciences*. 3rd ed. Elsevier, 676 pp.
- Woollings, T., A. Hannachi, and B. Hoskins, 2010: Variability of the North Atlantic eddy-driven jet stream. *Quart. J. Roy. Meteor. Soc.*, **136**, 856–868, <https://doi.org/10.1002/qj.625>.
- Xie, Z., Y. Du, and S. Yang, 2015: Zonal extension and retraction of the subtropical westerly jet stream and evolution of precipitation over East Asia and the western Pacific. *J. Climate*, **28**, 6783–6798, <https://doi.org/10.1175/JCLI-D-14-00649.1>.
- Yang, S., K.-M. Lau, and K.-M. Kim, 2002: Variations of the East Asian jet stream and Asian–Pacific–American winter climate anomalies. *J. Climate*, **15**, 306–325, [https://doi.org/10.1175/1520-0442\(2002\)015<0306:VOTEAJ>2.0.CO;2](https://doi.org/10.1175/1520-0442(2002)015<0306:VOTEAJ>2.0.CO;2).